ACSNANO

www.acsnano.org

ARTICLE

Multifunctional Magnetic Nanoclusters Can Induce Immunogenic Cell Death and Suppress Tumor Recurrence and Metastasis

Linlin Zhang,[#] Qingbo Zhang,[#] Daniel T. Hinojosa, Kaiyi Jiang, Quoc-Khanh Pham, Zhen Xiao, Vicki L. Colvin, and Gang Bao*

Cite This: *ACS Nano* 2022, 16, 18538–18554

Read Online

ACCESS | Metrics & More | Article Recommendations | Supporting Information

ABSTRACT: **Metastasis is the predominant cause of cancer deaths due to solid organ malignancies; however, anticancer drugs are not effective in treating metastatic cancer. Here we report a nanotherapeutic approach that combines magnetic nanocluster-based hyperthermia and free radical generation with an immune checkpoint blockade (ICB) for effective suppression of both primary and secondary tumors. We attached 2,2′-azobis(2-midinopropane) dihydrochloride (AAPH) molecules to magnetic iron oxide nanoclusters (IONCs) to form an IONC−AAPH nanoplatform. The IONC can generate a high level of localized heat under an alternating magnetic field (AMF), which decomposes the AAPH on the cluster surface and produces a large number of carbon-centered free radicals. A combination of localized heating and free radicals can effectively kill tumor cells under both normoxic and hypoxic conditions. The tumor cell death caused by the combination of magnetic heating and free radicals led to the release or exposure of various damage-associated molecule patterns, which promoted the maturation of dendritic cells. Treating the tumor-bearing mice with IONC−AAPH under AMF not only eradicated the tumors but also generated systemic antitumor immune responses. The combination of IONC−AAPH under AMF with anti-PD-1 ICB dramatically suppressed the growth of untreated distant tumors and induced long-term immune memory. This IONC−AAPH based magneto-immunotherapy has the potential to effectively combat metastasis and control cancer recurrence.**

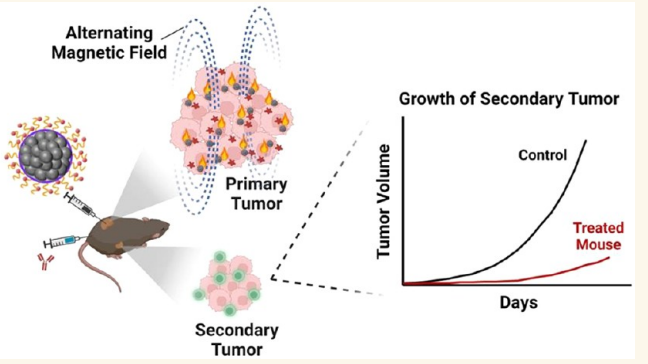

KEYWORDS: *magnetic nanoclusters, magnetic heating, free radicals, immunogenic cell death, cancer metastasis, immune checkpoint blockade*

Cancer remains a leading cause of death worldwide,[1] with the main cause of death being recurrence and metastasis after initial treatment of the primary tumor.[2,3] Unlike primary tumors, metastasis is a systemic disease. Conventional cancer therapeutics such as local surgery, chemotherapy, and radiation therapy have only had limited successes in preventing cancer relapse and metastasis.[4,5] The recent development of immunotherapy offers a means to treat metastatic disease.[6] For example, immune checkpoint blockade (ICB) therapy has been approved for clinical use in treating late-stage cancers.[7] However, the overall response rates to ICB therapy of solid tumors are relatively low. A large proportion of cancer patients cannot benefit from ICB therapy due to various reasons, such as low immunogenicity of the tumors, lack of tumor-infiltrating immune cells, and the immunosuppressive tumor microenvironment (TME).[8] Cell-based immunotherapies, including that based on T-cells and NK cells, have shown promise for treating hematological malignancies,[9,10] whereas evidence for effectively treating the metastatic disease of solid tumors is scant.[11] It has been shown that ICB therapy can be improved by combining it with other cancer treatment modalities that modulate tumor immunogenicity.[12]

Several cancer treatment modalities can cause immunogenic cell death (ICD), thus increasing the immunogenicity of solid tumor tissues and activating antitumor immunity.[13−16] Among these approaches, local hyperthermia therapies such as

Received: July 8, 2022
Accepted: October 24, 2022
Published: October 28, 2022

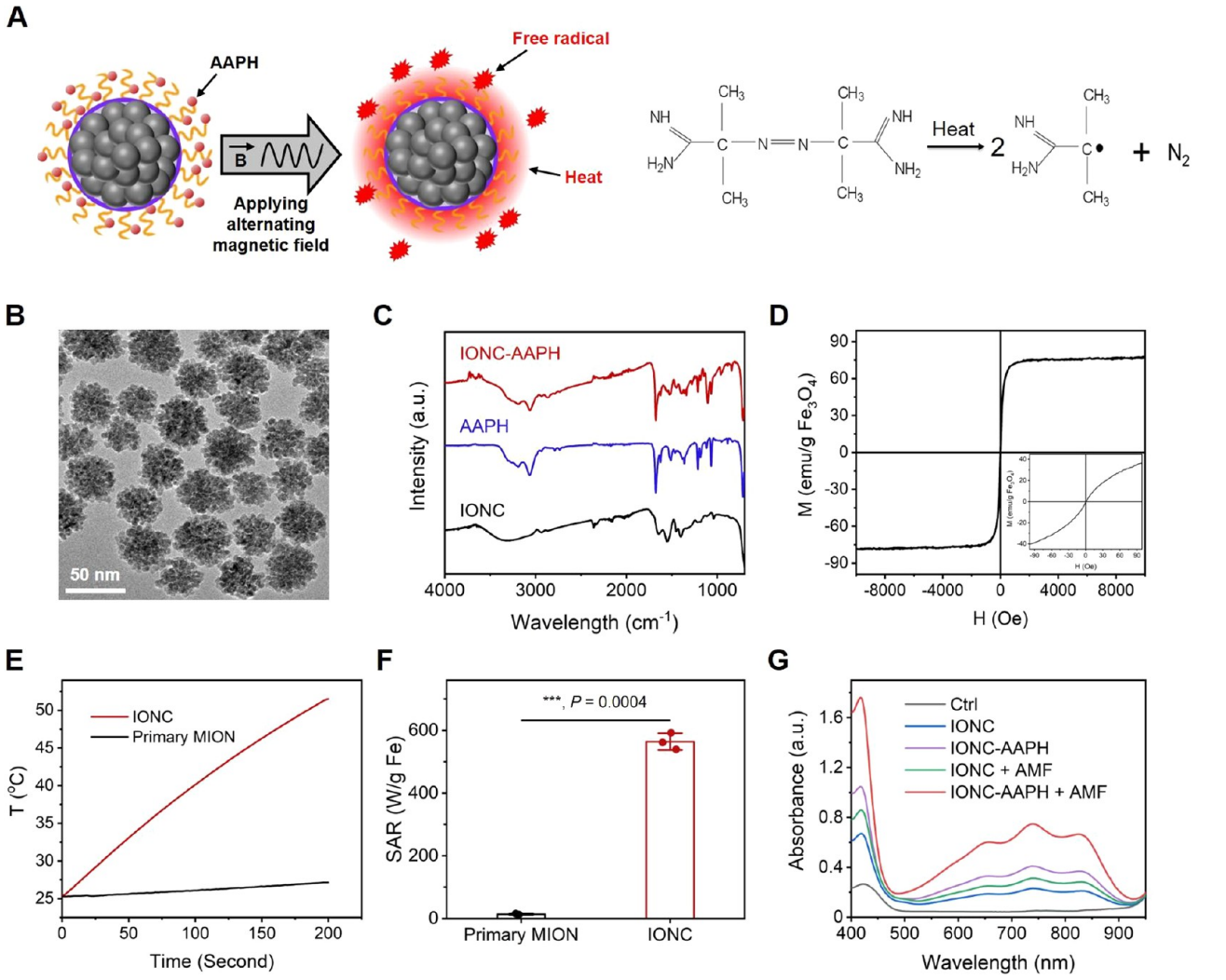

Figure 1. Structure and properties of IONC−AAPH. (A) Schematic illustration of heat and free radical generation from the multifunctional IONC−AAPH nanoplatform under AMF (left). Thermal decomposition of AAPH (right). (B) Representative TEM image of IONCs. (C) FTIR spectra of IONC−AAPH, AAPH, and IONC. (D) Magnetization curves of IONC−AAPH. Inset: zoom-in view of the magnetization curve from −100 to +100 Oe. (E) Heating profiles of IONCs and primary magnetic iron oxide nanocrystals (MIONs) at 0.5 mg Fe/mL in water. (F) Specific absorption rate (SAR) of IONCs and primary MIONs measured under AMF of 9.35 kA/m and 320 kHz. Data represent mean ± s.d. ***P < 0.001 based on one-tailed Student's t-test. (G) Generation of ABTS+· under different conditions.

photothermal therapy and magnetic heating offer potential advantages due to minimal invasiveness and low side effects.[17] However, photothermal therapy requires effective delivery of local heat to the tumor tissue by light.[18−21] Due to attenuation by biological tissue, light can only penetrate shallow tissues, thus rendering the use of photothermal therapy in treating tumors in deep tissue impractical.[22] In contrast, magnetic heating provides an attractive approach for cancer hyperthermia therapy since the applied magnetic field has essentially unlimited penetration depth in biological tissues.[23−26] One major challenge for magnetic hyperthermia is the low magnetothermal efficiency of magnetic iron oxide nanoparticles.[27] It is often used as an adjuvant treatment to sensitize tumors to radiation therapy or chemotherapy.[28]

To increase the efficacy of magnetic hyperthermia therapy and eradicate both primary and metastatic tumors, we have developed a combination therapeutic approach, magneto-immunotherapy, that combines magnetic hyperthermia, free radical generation, and immune checkpoint blockade therapy for cancer treatment. It has been demonstrated that free radicals can modulate tumor immunogenicity.[16,29] In particular, reactive oxygen species (ROS) generated by radiation or light can cause immunogenic cell death, thus priming antitumor immune responses.[30−33] However, the production of ROS from these therapeutic modalities is often hindered by low oxygen levels in the tumor microenvironment (TME), limiting their effectiveness.[34,35] It has been shown that upon heating an azo compound can decompose to generate carbon-centered free radicals quickly without the need of oxygen.[36−39] In our study, we loaded magnetic iron oxide nanocrystal clusters (IONC) with water-soluble azo compound 2,2′-azobis(2-amidinopropane) dihydrochloride (AAPH), which decomposes by heat generated from IONC under an applied alternating magnetic field (AMF), resulting in carbon-centered free radicals. It has been shown in cell culture that free radicals generated from the decomposition of AAPH can sensitize cancer cells to heat and enhance heat-induced cancer cell killing.[40−42] We demonstrated that the simultaneous generation of localized heat and free radicals can induce immunogenic cell death and efficiently eradicate the primary

https://doi.org/10.1021/acsnano.2c06776
ACS Nano 2022, 16, 18538−18554

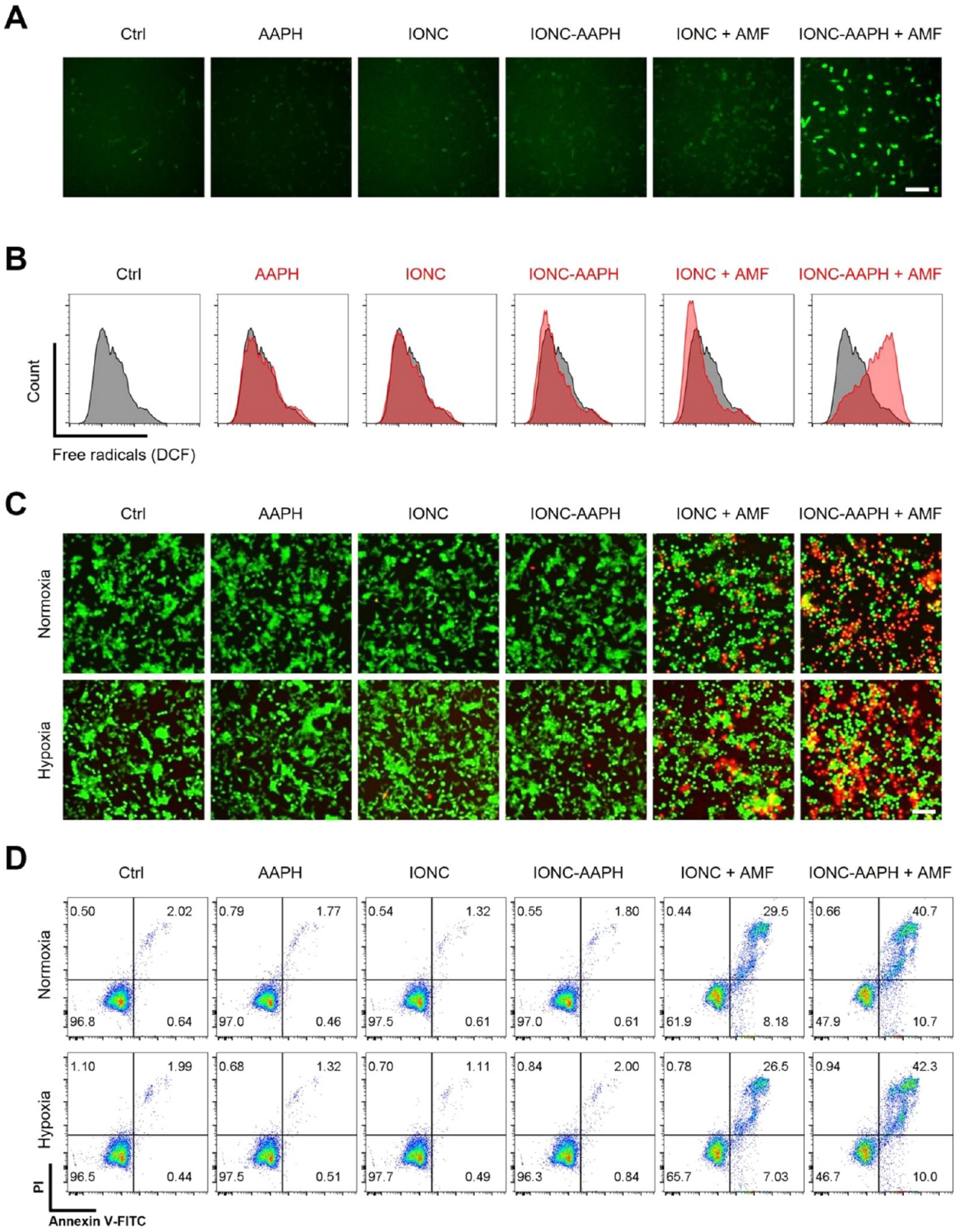

Figure 2. Free radical generation and cell killing effect of IONC−AAPH *in vitro*. (A,B) Fluorescence images (A) and flow cytometry analysis (B) of intracellular free radicals in MC-38 cells via fluorescence from DCF. Scale bar, 100 μm. (C) Fluorescence images of MC-38 cells costained with calcein AM (live cells, green) and propidium iodide (dead cells, red) after different treatments under normoxic and hypoxic conditions. Scale bar, 100 μm. (D) Flow cytometry analysis of cell death in MC-38 cells after different treatments under normoxic and hypoxic conditions.

tumors at low dose of nontoxic IONCs under the clinically safe AMF. When the use of local heat and free radical generation is combined with ICB, the resulting magneto-immunotherapy has shown efficient abscopal effect and long-term immune

https://doi.org/10.1021/acsnano.2c06776
ACS Nano 2022, 16, 18538−18554

memory, thus demonstrating the potential in improving ICB therapy and suppressing tumor recurrence and metastasis. Compared with light-based methods, such as photothermal therapy and photodynamic therapy, the magneto-immunotherapy developed in this study can treat primary and distant tumors in deep tissue since a magnetic field can be applied to the whole body.

RESULTS AND DISCUSSION

Synthesis and Characterization of IONC−AAPH. As shown in Figure 1A, the nanotherapeutic agent we synthesized, IONC−AAPH, is composed of magnetic iron oxide nanocrystal clusters (IONCs) and AAPH, in which IONCs were used as the heating source for magnetic hyperthermia and for decomposing AAPH to generate carbon-centered free radicals (Figure 1A). The IONCs were synthesized through the hydrolysis of iron salts in glycol in a solvothermal reaction. Figure 1B shows a typical transmission electron microscopy (TEM) micrograph of the IONCs. The diameter of IONCs determined from the TEM images was 40 ± 3.9 nm. Each nanocluster is composed of ∼300 primary magnetic iron oxide nanocrystals (MIONs) of ∼5 nm. The primary nanoparticles in each nanocluster have the same crystal orientations. The specific surface area of the nanoclusters measured by a Brunauer−Emmett−Teller (BET) surface analyzer is around half of the specific surface area of primary 5 nm MIONs, suggesting that the neighboring primary nanoparticles within an IONC have a lot of shared interfaces, thus interconnected. The Raman spectrum of IONCs indicates that the primary MIONs are magnetite (Fe_3O_4). The IONCs were coated with poly(AA-*co*-AMPS-*co*-PEG), rendering them water-soluble and stable in cell culture media.

To produce free radicals, we loaded a water-soluble azo compound AAPH to the IONC surface through a poly(acrylic acid) (PAA) chain. It has been shown that other azo compounds in photothermal agents can generate oxygen-independent free radicals under laser.[22,38,39] In brief, PAA was first reacted with a nitrodopamine molecule to form nitrodopamine-PAA. The AAPH molecules were then conjugated to nitrodopamine-PAA through reaction between the amine group on AAPH and the carboxyl group on PAA. The nitrodopamine-PAA-AAPH was attached to the IONC surface through the coordination between the catechol group on the nitrodopamine molecule and the iron atoms on the nanocluster surface. The successful loading of AAPH to the IONCs was confirmed by the spectra from Fourier transform infrared (FTIR) spectroscopy (Figure 1C). Compared with conventional magnetic iron oxide nanocrystals, the IONCs exhibit superior magnetic properties due to their nanostructure.[43] The magnetization curve shows negligible coercivity, confirming that the 40 nm IONCs remain superparamagnetic (Figure 1D). We found that the IONCs (at 0.5 mg Fe/mL concentration) can generate heat rapidly under AMF of 9.35 kA/m and 320 kHz (the same AMF was used throughout the study), resulting in a temperature increase of 25 °C in water within 200 s (Figure 1E). The specific absorption rate (SAR) of the 40 nm IONCs was 564 ± 27 W/g Fe, which was 40-fold higher than that of the primary MIONs (Figure 1F). To determine if heat from IONCs under AMF can decompose AAPH to generate free radicals,[44] we used 2,2′-azobis(2-methylpropionamidine) dihydrochloride (ABTS) as a free radical indicator. ABTS reacts with free radicals and forms $ABTS^{+\bullet}$, which exhibits a characteristic absorbance spectrum between 400 and 950 nm, with a peak at 734 nm. PBS containing IONC or IONC−AAPH of 300 μg Fe/mL concentration was mixed with ABTS solution and then incubated at 37 °C or subjected to AMF for 1 h, followed by removal of the nanoclusters from the samples using centrifugal filters. The generation of $ABTS^{+\bullet}$ was then determined by measuring the absorbance spectra of the samples. As shown in Figure 1G and Supplementary Figure S1, for the sample with IONC−AAPH under AMF, the absorbance peak at 734 nm due to $ABTS^{+\bullet}$ was significantly higher than that of other groups (PBS as control, IONC, IONC−AAPH without AMF, and IONC under AMF), indicating free radical generation due to decomposition of AAPH.

Intracellular Free Radical Generation. We further investigated the intracellular free radical generation of IONC−AAPH using 2′,7′-dichlorodihydrofluorescein diacetate (H_2DCFDA) as an intracellular free radical probe. H_2DCFDA is a nonfluorescent cell-permeant compound. Upon oxidation by free radicals, H_2DCFDA is converted to highly fluorescent 2′,7′-dichlorofluorescein (DCF). MC-38 cells (murine colon adenocarcinoma cell line) were preincubated with IONC or IONC−AAPH (at 300 μg Fe/mL concentration, same for all cellular studies) for 1 h to allow internalization into cells. The intracellular IONC and IONC−AAPH were 0.79 ± 0.16 and 0.87 ± 0.12 pg Fe/cell, respectively, as quantified by a ferrozine-based colorimetric assay. After internalization, the cells were exposed to AMF for 1 h. The intracellular free radicals in MC-38 cells were then examined with H_2DCFDA through fluorescence microscopy and flow cytometry. We found that MC-38 cells treated with IONC−AAPH under AMF showed bright green fluorescence signal, as demonstrated by both fluorescence microscopy and flow cytometry, whereas there was only low background green fluorescence in cells only (as control), and cells treated with free AAPH, IONC, IONC−AAPH, or IONC under AMF (magnetic hyperthermia) (Figure 2A,B, Supplementary Figure S2). These results clearly indicate that IONC−AAPH can generate a high level of free radicals in cells under AMF.

***In Vitro* Tumor Cell Killing.** To determine the ability of IONC−AAPH to kill tumor cells, MC-38 cells were treated with IONC−AAPH and subjected to AMF for 2 h under normal level of oxygen (normoxia), and the cell death was imaged fluorescently (Figure 2C) by costaining cells with calcein AM (for live cells) and propidium iodide (PI, for dead cells). Cell death was further quantified by flow cytometry analysis of Annexin-V and PI double-stained cells (Figure 2D). We found that under AMF, IONC−AAPH caused a higher level of cell death compared with IONC only (52.1% vs 38.1% as quantified by flow cytometry in Figure 2D). Without AMF, IONC−AAPH did not kill MC-38 cells, indicating a good biocompatibility (Figure 2C,D). We also determined the cell-killing ability of IONC−AAPH under hypoxic condition by pretreating MC-38 cells with 100 μM $CoCl_2$ for 24 h.[45] Hypoxia was successfully induced as evidenced by the upregulation and accumulation of hypoxia-inducible factor 1-α (HIF-1α) (Supplementary Figure S3). As shown in Figure 2C,D, under hypoxia, IONC−AAPH maintained a higher cell-killing ability than IONC alone (53.3% vs 34.3% as quantified by flow cytometry in Figure 2D). These results suggest that magnetic heating and the carbon-centered free radical from AAPH can kill tumor cells effectively and synergistically, even under hypoxic conditions. Since carbon-centered free radicals

https://doi.org/10.1021/acsnano.2c06776
ACS Nano 2022, 16, 18538−18554

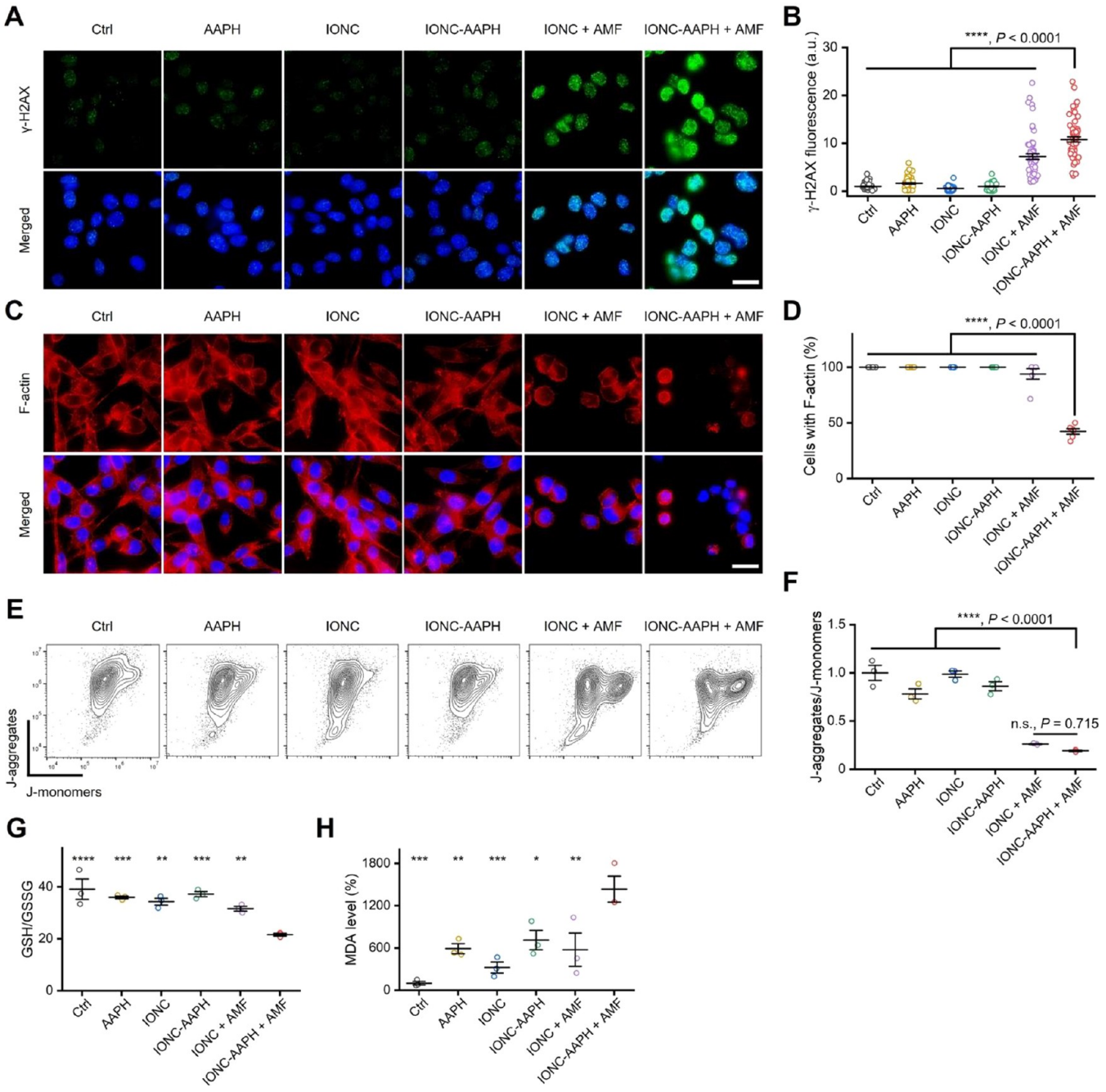

Figure 3. Mechanisms of IONC−AAPH-mediated cell killing. (A) γ-H2AX foci analysis of DNA damage 4 h after treatment. Green, γ-H2AX foci; blue, nuclei. Scale bar, 100 μm. (B) Quantification of fluorescence staining of γ-H2AX in (A). *n* = 60 cells for each group. (C) Imaging of F-actin structure in MC-38 cells by phalloidin staining of actin filaments 4 h after treatment. Red, F-actin; blue, nuclei. Scale bar, 100 μm. (D) Quantification of the percentage of cells with F-actin structure as shown in (C). *n* = 6 fields for each group. (E) Flow cytometry analysis of mitochondrial membrane potential of MC-38 cells 4 h after treatment by JC-1 staining. (F) Quantification of the J-aggregate to J-monomer ratio using the mean fluorescence detected by flow cytometry in (E). (G) GSH depletion measurement of MC-38 cells 2 h after treatment. (H) Quantification of MDA levels in MC-38 cells 2 h after treatment. Data represent means ± s.e.m. Statistical analysis was performed using one-way ANOVA with posthoc Dunnett's multiple comparisons test, compared with the IONC−AAPH + AMF group. *P < 0.05, **P < 0.01, ***P < 0.001, and ****P < 0.0001. n.s., not significant.

from AAPH can be indued by heat independent of oxygen, our approach using IONC−AAPH has a clear advantage over therapeutic strategies based on ROS generation by radiation or light, which is often hindered by the low oxygen levels in the TME.[34,35]

IONC−AAPH under AMF Induced Damage to Multiple Cellular Components. It has been reported that hyperthermia treatment can induce lipid peroxidation, DNA damage, protein denaturation, and cell organelle disruption.[46−48] Previous studies have shown that the carbon-centered free radicals generated from AAPH are highly reactive and can also damage lipid, DNA, protein, and other biomolecules, leading to cell death.[49] Thus, to understand cell death caused by IONC−AAPH under AMF, we evaluated the effects of IONC−AAPH on various cellular components,

https://doi.org/10.1021/acsnano.2c06776
ACS Nano 2022, 16, 18538−18554

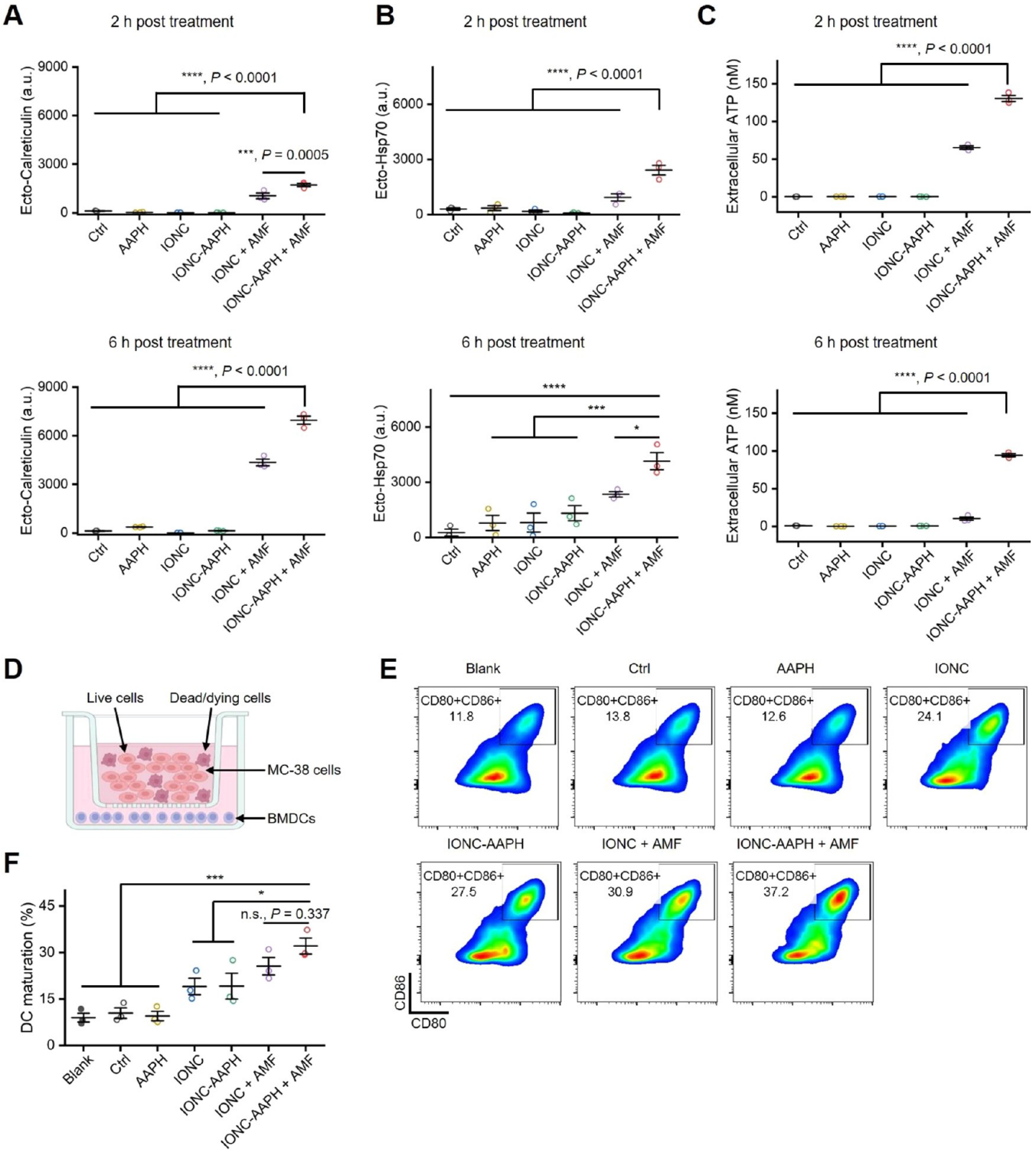

Figure 4. Immunogenic cell death and dendritic cell maturation induced by IONC−AAPH-mediated magnetotherapy. (A−C) Induction of damage-associated molecular patterns (DAMPs). (A) Quantification of cell surface-exposed calreticulin (ecto-calreticulin) on MC-38 cells 2 and 6 h after treatment. (B) Quantification of cell surface-exposed Hsp70 (ecto-Hsp70) on MC-38 cells 2 and 6 h after treatment. (C) Quantification of ATP release from MC-38 cells 2 and 6 h after treatment. (D−F) Activation of dendritic cells. (D) Schematic illustration of the transwell coculture experiment. MC-38 cells were added to the upper chamber of the transwell system immediately after treatment, and cocultured with BMDCs in the lower chamber for 24 h. (E,F) The quantification of DC maturation by flow cytometry (n = 3). The percentage of DC maturation was calculated as the frequency of mature DCs ($CD80^+CD86^+$) in all BMDCs ($CD11c^+$). The blank groups are BMDCs only. Representative flow cytometry data are shown in (E), and quantification data are shown in (F). Data represent mean ± s.e.m. Statistical analysis was performed using one-way ANOVA with posthoc Dunnett's multiple comparisons test, compared with the IONC−AAPH + AMF group. *P < 0.05, ***P < 0.001, and ****P < 0.0001. n.s., not significant.

https://doi.org/10.1021/acsnano.2c06776
ACS Nano 2022, 16, 18538−18554

including DNA, F-actin, mitochondria, glutathione (GSH), and lipid.

We used γ-H2AX as a marker of DNA damage which forms foci around the site of DNA double-strand breaks (DSB).[50] As shown in Figure 3A, treating MC-38 cells with IONC under AMF induced γ-H2AX foci formation, indicating DNA damage due to IONC-mediated hyperthermia. When combined with free radical generation, i.e., treating cells with IONC−AAPH under AMF for 90 min, the foci number and fluorescence intensity were increased dramatically (Figure 3A). Shown in Figure 3B is the quantification of γ-H2AX expression based on the fluorescence intensity, indicating that combined heat and free radical generation by IONC−AAPH has caused higher DNA damage compared with hyperthermia alone. The very low numbers of γ-H2AX foci observed in the four control groups (cells only, AAPH, IONC, and IONC−AAPH without AMF) are likely due to the spontaneous DNA damage in the MC-38 cells, as spontaneous γ-H2AX foci have also been found in several cancer cell lines and some cancer tissues.[51,52]

To examine the effect of heating and free radicals on the actin cytoskeleton, we stained actin filaments (F-actin) with fluorescent phalloidin. Without heating, F-actin in cells treated with AAPH, IONC, and IONC−AAPH was well organized and elongated, similar to cells-only as control (Figure 3C). The MC-38 cells treated with IONC and subjected to AMF (magnetic hyperthermia) rounded up and showed retracted actin filaments. In contrast, for cells treated with IONC−AAPH and subjected to AMF, more than 50% of them lost the F-actin structure (i.e., no phalloidin staining) (Figure 3C,D), suggesting that the actin filaments in these cells were disrupted by the combination of heat with free radicals. In cells subjected to heating and free radicals but still showing phalloidin staining, the actin filaments were further retracted and more condensed compared with cells under heating only (Figure 3C).

We also examined the effect of heat and free radical generation by IONC−AAPH on mitochondria with JC-1 dye, which is an indicator of mitochondrial membrane potential (MMP).[53] In healthy cells with high MMP, JC-1 accumulates in the mitochondria and forms J-aggregates, which emit red fluorescence.[53] In contrast, in apoptotic cells with low MMP, JC-1 diffuses in the cytoplasm and remains as J-monomers, resulting in green fluorescence.[53] A decrease in J-aggregates (red) to J-monomers (green) ratio indicates loss of MMP, i.e., mitochondrial depolarization.[53] J-aggregates (red) were formed in the control cells and cells treated with AAPH, IONC, and IONC−AAPH (without heating or free radicals) as shown by the fluorescent images (Supplementary Figure S4). In contrast, there were only J-monomers (green) in the cells treated with IONC or IONC−AAPH under AMF, suggesting that depolarization of mitochondria occurred due to heat or the combination of heat and free radicals (Supplementary Figure S4). The J-aggregates to J-monomers ratios quantified using flow cytometry confirmed the significant MMP loss due to heat and free radicals (Figure 3E,F). No significant difference was observed between having heat only and having heat plus free radicals (Figure 3F), suggesting that it was mainly magnetic heating that caused mitochondrial depolarization in MC-38 cells.

Glutathione (GSH) is an antioxidant that plays an important role in scavenging of intracellular free radicals and protecting cells against oxidative damage.[54] GSH depletion disrupts the redox homeostasis and leads to oxidative stress and eventual cell death.[55] After adding 300 μg Fe/mL of IONC or IONC−AAPH to cell culture media, MC-38 cells were subjected to AMF for 2 h. These cells were then incubated at 37 °C for another 2 h before the intracellular GSH was quantified. Intracellular GSH was also measured for cells treated with AAPH, IONC, or IONC−AAPH, respectively, without AMF and incubated at 37 °C for 4 h. The intracellular GSH was quantified using a luminescence-based GSH-Glo glutathione assay. Figure 3G shows that treating MC-38 cells with free AAPH, IONC, and IONC−AAPH, respectively, did not affect the GSH to GSSG ratio, and magnetic hyperthermia (IONC with AMF) only caused a slight decrease in GSH/GSSG. In contrast, treating cells with IONC−AAPH under AMF (i.e., with both heating and free radicals) decreased the GSH/GSSG ratio to 55% of that in the control cells (Figure 3G). These results suggest that IONC−AAPH under AMF can cause significant GSH depletion and thus an increased level of oxidative stress.

We further quantified the effect of IONC−AAPH-induced heat and free radicals on lipids by measuring the level of malondialdehyde (MDA), which is one of the final products of lipid peroxidation and has been widely used as a biomarker of oxidative stress.[56] We found that the MC-38 cells treated with free AAPH, IONC, and IONC−AAPH, respectively, without AM, as well as cells treated with IONC under AMF had some increase in MDA levels compared with that of control cells (Figure 3H). The low levels of lipid peroxidation in these groups were likely caused by the free radicals generated from the slow decomposition of AAPH at 37 °C, or the IONC-induced fenton/fenton-like reaction, or their combination (IONC−AAPH without AMF). Cells treated with IONC−AAPH under AMF induced a significant increase in the MDA level (Figure 3H). Our results indicate that heat and free radicals generated by IONC−AAPH induced lipid peroxidation, which in turn caused cancer cell death.

Taken together, we have demonstrated that IONC−AAPH under AMF can cause damage to multiple cellular components, including DNA (Figure 3A,B), actin cytoskeleton (Figure 3C,D), mitochondria (Figure 3E,F, Supplementary Figure S4), and lipid membranes (Figure 3H), as well as significant intracellular GSH depletion (Figure 3G). All of these contributed to the cancer cell death triggered by IONC−AAPH.

IONC−AAPH under AMF Caused Immunogenic Cell Death and Dendritic Cell Maturation. Immunogenic cell death (ICD) is characterized by the exposure or release of damage-associated molecular patterns (DAMPs), such as calreticulin (CRT), heat shock protein 70 (Hsp70), and adenosine triphosphate (ATP).[57] To determine if IONC−AAPH under AMF induces immunogenic cell death, we examined, respectively, the cell surface translocation of CRT (ecto-CRT) and Hsp70 (ecto-Hsp70) and the release of ATP to extracellular space at different time points after treating MC-38 cells with IONC or IONC−AAPH under AMF for 2 h or with AAPH, IONC, or IONC-AAPH without AMF (defined as "treatment" here and in Figure 4). Our results show that the translocation of CRT and Hsp70 to the cell surface happened within 2 h after treatment with IONC and IONC−AAPH under AMF (Figure 4A,B, Supplementary Figures S5A, S6A). At 6 h post-treatment, the ecto-CRT and ecto-Hsp70 levels of MC-38 cells treated with heating and free radicals were still significantly higher than those of other groups (cells only, AAPH, IONC and IONC−AAPH without AMF, and IONC

https://doi.org/10.1021/acsnano.2c06776
ACS Nano 2022, 16, 18538−18554

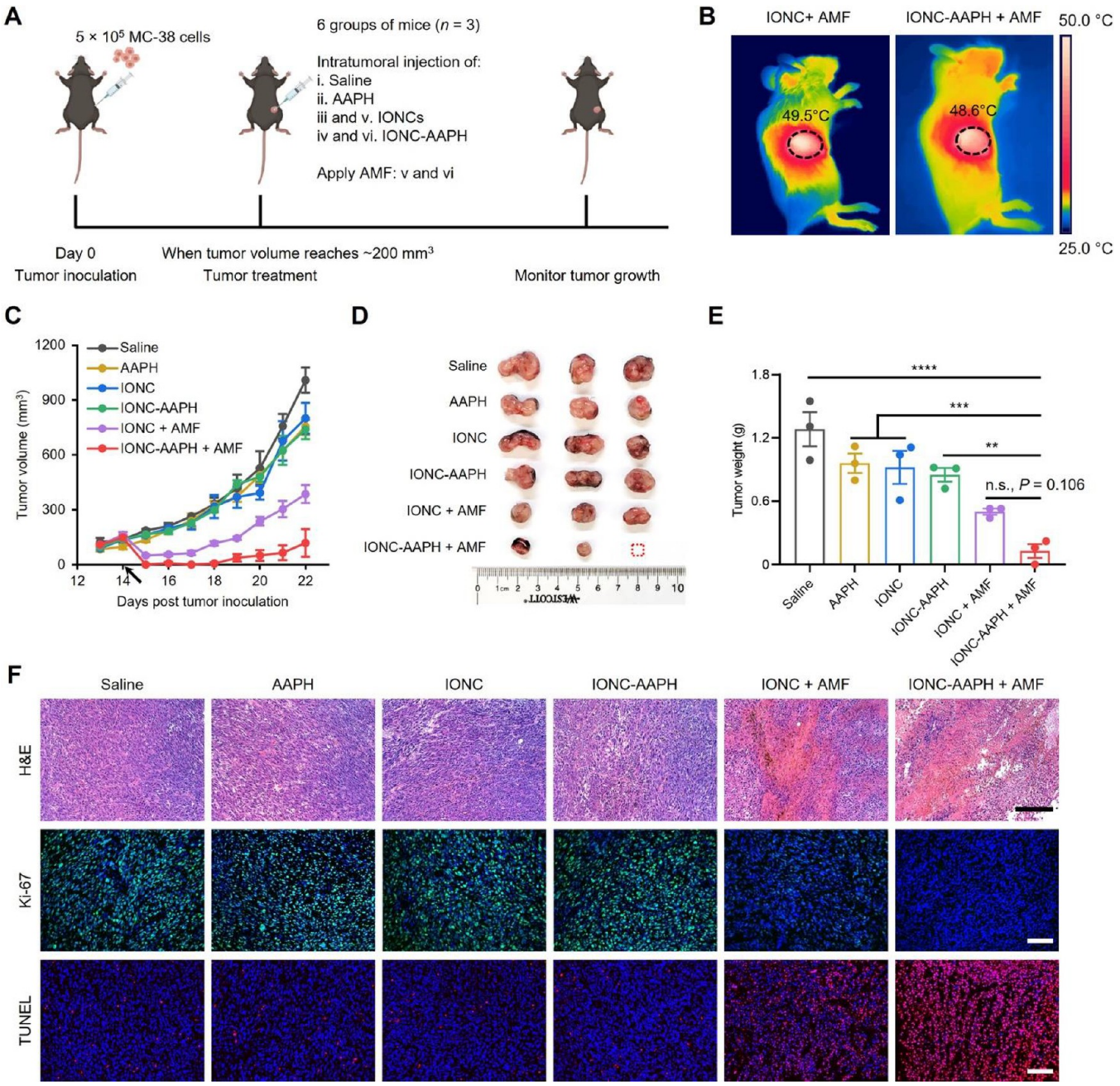

Figure 5. ***In vivo*** **antitumor activity of IONC−AAPH-mediated magnetotherapy. (A) Schematic illustration of the experimental design. (B) Representative IR images of MC-38-tumor-bearing mice after the treatment. Black dashed circles, tumors. (C) Tumor growth curves of different treatment groups. The black arrow indicates the onset of treatment. (D) Images of excised tumors at the end point. (E) Weights of excised tumors. Data represent means ± s.e.m. Statistical analysis was performed using one-way ANOVA with posthoc Dunnett's multiple comparisons test, compared with the IONC−AAPH + AMF group. *****P*** **< 0.01, ******P*** **< 0.001, and *******P*** **< 0.0001. n.s., not significant. (F) H&E, Ki-67, and TUNEL staining of tumor sections 24 h after treatment. In Ki-67 (green) and TUNEL (red) staining, the nuclei were stained with DAPI (blue). Scale bar, 100 μm.**

with AMF) (Figure 4A,B, Supplementary Figures S5B, S6B). Additionally, 24 h after treatment with IONC−AAPH, the expression of Hsp70 protein increased by 27-fold compared with control (Supplementary Figure S7). We further found that there was a high level of extracellular ATP due to heat and free radicals. At 2 h post-treatment with IONC−AAPH, the concentration of extracellular ATP was 130.4 nM, ∼420-fold higher than that of cells only (control) (Figure 4C). At 6 h post-treatment with IONC−AAPH, the level of extracellular ATP was still ∼100-fold higher than the control. Heating only without free radicals also showed significant increase in extracellular ATP, ∼210-fold and ∼11-fold higher than control, respectively, at 2 and 6 h post-treatment (Figure 4C). Our results suggest that the cell death due to IONC−AAPH under AMF is highly immunogenic.

Dendritic cells (DCs) are a key type of antigen-presenting cells that play critical roles in initiating and regulating antitumor immune response. To determine if the immunogenic cell death induced by magnetotherapy can activate dendritic cells, we cocultured bone marrow-derived dendritic

https://doi.org/10.1021/acsnano.2c06776
ACS Nano 2022, 16, 18538−18554

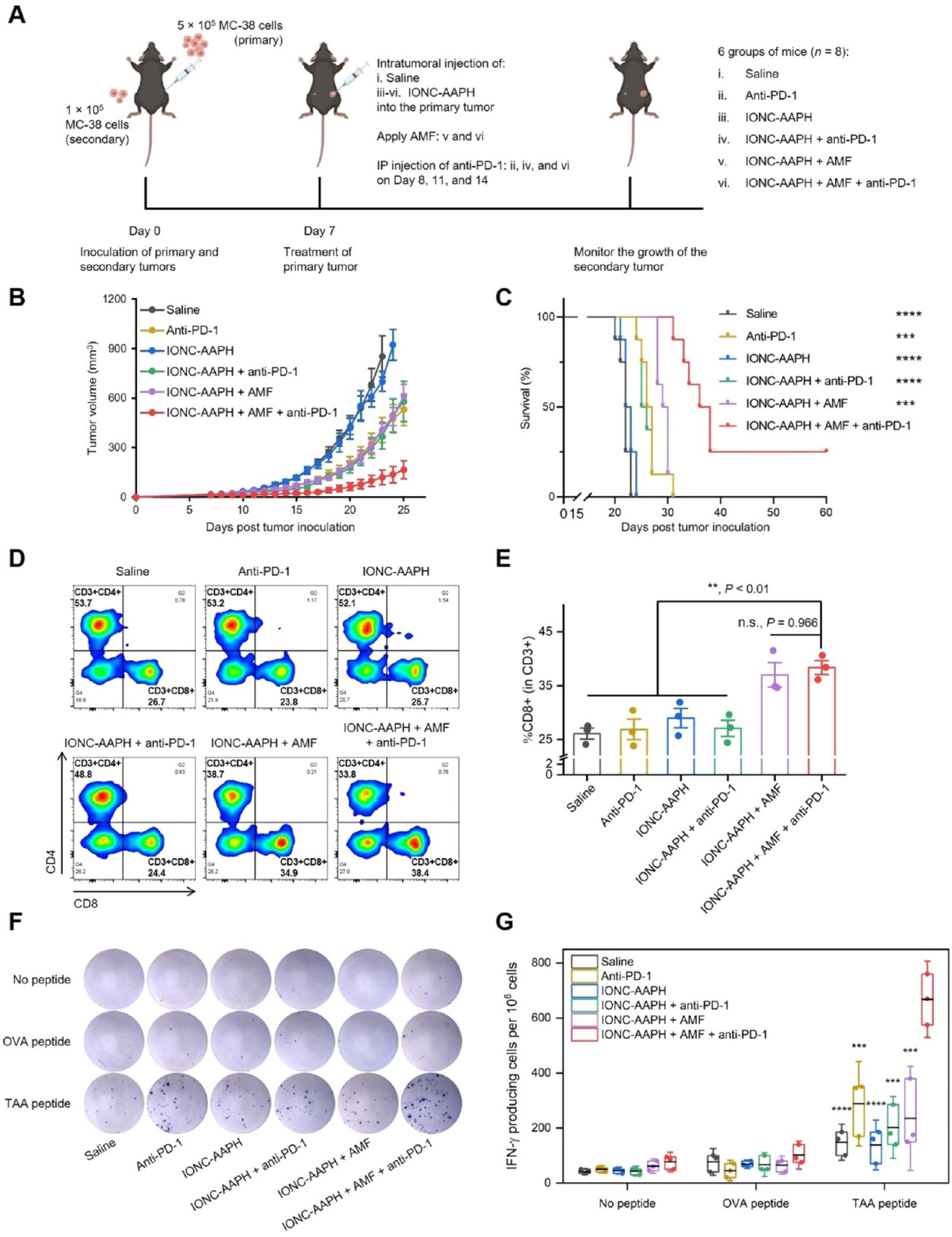

Figure 6. Abscopal effect of magneto-immunotherapy. (A) Schematic illustration of the experiment design. (B) Average growth curve of secondary tumor. (C) Survival curves of mice receiving different treatments. n = 8. (D,E) Infiltrating immune cells in the secondary tumors (n = 3). Representative flow cytometry data are shown in (D), and quantification data are shown in (E). (F,G) Tumor antigen-specific T cells determined by ELISpot assay (n = 3). IFN-γ secreting T cells were detected 24 h after stimulation. Splenocytes without peptide stimulation were included as control groups. Representative spots are shown in (F), and quantification data are shown in (G). Data represent mean ± s.e.m. Statistical analysis was performed using log-rank Mantel-Cox test (C) or one-way ANOVA with posthoc Dunnett's multiple comparisons test (E,G), compared with the IONC−AAPH + AMF + anti-PD-1 group. **P < 0.01, ***P < 0.001, and ****P < 0.0001. n.s., not significant.

https://doi.org/10.1021/acsnano.2c06776
ACS Nano 2022, 16, 18538−18554

cells (BMDCs) with IONC−AAPH-treated MC-38 cells, together with the medium containing DAMPs, in a transwell system for 24 h (Figure 4D). The maturation of dendritic cells was estimated as the percentage of $CD80^+CD86^+$ cells in $CD11c^+$ cells (Supplementary Figure S8). As shown in Figure 4E,F, MC-38 cells alone or the cells treated by AAPH did not show a noticeable effect on DC maturation. The percentage of mature DCs in IONC and IONC−AAPH groups was 2.1-fold of the blank. Given that incubation with IONC and IONC−AAPH had little effect on MC-38 cells (Figures 2, 3, and 4A−C), the increase of DC maturation with these two groups without AMF was likely induced by the internalized nanoclusters, since the stimulatory effect of nanomaterials on DC maturation has been reported.[58] The DC maturation in magnetic hyperthermia group (IONC + AMF) and magnetotherapy group (IONC−AAPH + AMF) was 2.8- and 3.6-fold of the blank, respectively (Figure 4F). The significantly increased DC maturation in the magnetotherapy group indicates that the immunogenic cell death caused by IONC−AAPH under AMF can effectively activate DCs.

IONC−AAPH under AMF Generated High Anti-Tumor Activity *In Vivo*. We evaluated the antitumor activity of IONC−AAPH *in vivo* with a subcutaneous MC-38 mouse tumor model. The subcutaneous tumor was induced by inoculating MC-38 cells into the right flank of the C57BL/6N mouse (Figure 5A). The mice were randomly divided into 6 groups (n = 3): (i) saline, (ii) AAPH, (iii) IONC, (iv) IONC−AAPH, (v) IONC + AMF, and (vi) IONC−AAPH + AMF. When the tumor volume reached 150−200 mm^3, the mice were intratumorally injected with saline, AAPH (2 mM), IONC (5 mg Fe/mL), and IONC−AAPH (5 mg Fe/mL), respectively (Figure 5A). After injection the mice in IONC + AMF and IONC−AAPH + AMF groups were subjected to AMF for 1 h. The temperature of the tumors injected with IONC or IONC−AAPH increased rapidly and reached above 45 °C within 5 min, as measured by an infrared thermal camera (Supplementary Figure S9A,C,G). After applying AMF, the temperature in the tumor was much higher than in other parts of the body (Figure 5B, Supplementary Figure S9B,D). In contrast, a negligible temperature increase was observed in the tumors injected with saline and treated with AMF (Supplementary Figure S9E−G).

As shown in Figure 5C and Supplementary Figure S10, IONC-induced hyperthermia (IONC + AMF) reduced the tumor burden effectively and delayed the regrowth of tumor from the residual tumor cells. When combining local heating with free radical generation by IONC−AAPH under AMF, tumor growth was significantly inhibited, much more than hyperthermia alone. Specifically, at the end point (Day 22), the average tumor volume in mice treated with IONC−AAPH under AMF was reduced by 88.2% compared with control tumors (injected with saline), whereas with IONC alone under AMF the average reduction in tumor volume was only 61.7% (Figure 5C). The reduction of tumor weight due to heat and free radicals generated by IONC−AAPH was higher than hyperthermia alone, while injecting AAPH, IONC, and IONC−AAPH without applying AMF only slightly reduced the tumor weight (Figure 5D,E). The clear synergy between heat from IONC under AMF and free radicals generated from AAPH is likely due to free radicals sensitizing the tumor cells to heat thus enhancing heat-induced cell killing, similar to the combination of photothermal therapy (PTT) and photodynamic therapy (PDT) that kill tumor cells by heat and free radicals induced by light.[59−62]

The hematoxylin and eosin (H&E) staining and terminal deoxynucleotidyl transferase dUTP nick end labeling (TUNEL) analysis of the tumor tissues demonstrated that injecting IONC−AAPH and applying AMF caused significant tumor tissue damage, higher than hyperthermia alone; no tumor tissue damage was found in the control groups (injecting saline, AAPH, IONC, IONC−AAPH without AMF) (Figure 5F). In addition, the analysis of Ki-67 expression in tumor tissues indicates that tumor cell proliferation was inhibited efficiently by IONC−AAPH under AMF (Figure 5F). Taken together, our results suggest that the combination of local heat and free radicals by IONC−AAPH led to a profound antitumor effect *in vivo*.

Magneto-Immunotherapy Induced Strong Abscopal Effect. We next determined whether magneto-immunotherapy that combines IONC−AAPH-based local heat and free radical generation with anti-PD-1 immune checkpoint blockade (ICB) therapy can induce an abscopal antitumor effect. Over the past a few decades, several local cancer treatment modalities, such as radiation therapy and phototherapy, have been reported to induce an abscopal effect on the untreated distant tumors.[63,64] Previous studies have shown that the abscopal effect is attributed to the systemic antitumor immune responses triggered by immunogenic cell death during local treatment[65] and combining local treatment stratagies with immunotherapy can amplify the abscopal effect.[63,66]

Our *in vitro* studies have demonstrated the ability of IONC−AAPH to induce immunogenic cell death (Figure 4, Supplementary Figures S5−7). To determine the abscopal effect, we used a biliteral subcutaneous tumor model by inoculating MC-38 cells into the right and left flanks of the same mouse, as shown in Figure 6A. The tumor on the right side was designated as the primary tumor, subjected to different treatment, and the tumor on the left side was designated as secondary (distant) tumor without any treatment. The mice were randomly divided into 6 groups (n = 8): (i) saline, (ii) anti-PD-1, (iii) IONC−AAPH, (iv) IONC−AAPH + anti-PD-1, (v) IONC−AAPH + AMF, and (vi) IONC−AAPH + AMF + anti-PD-1. When the volume of the primary tumor reached 50−100 mm^3, saline or IONC−AAPH was injected directly into the primary tumor. Mice in groups (v) and (vi) were treated with IONC−AAPH under AMF for 1 h. For mice in groups (ii), (iv), and (vi), anti-PD-1 antibody was injected intraperitoneally at 10 mg/kg of body weight on Days 8, 11, and 14 (Figure 6A). The tumor growth was monitored daily.

As expected, injecting IONC−AAPH into the primary tumor without AMF showed no inhibitory effect on the secondary tumor (Figure 6B, Supplementary Figure S11). In contrast, injecting IONC−AAPH into the primary tumor and subjecting the mice to AMF partially inhibited the growth of the secondary tumor, suggesting a moderate abscopal effect due to local heat and free radical generation (Figure 6B, Supplementary Figure S11). When combining heat and free radical produced by IONC−AAPH with anti-PD-1 ICB, the abscopal effect on the secondary tumor was dramatically enhanced, as demonstrated by the much slower growth of the secondary tumor compared with the saline control group (Figure 6B, Supplementary Figure S11). Note that injection of anti-PD-1 antibody also partially delayed the growth of the secondary tumor due to the activation of systemic immune

https://doi.org/10.1021/acsnano.2c06776
ACS Nano 2022, 16, 18538−18554

response (Figure 6B, Supplementary Figure S11). However, all the animals injected with anti-PD-1 antibodies reached the end point within 31 days (Figure 6C). In comparison, the combination of local heat, free radicals, and anti-PD-1 ICB eradicated both the primary and secondary tumors in 25% of the treated mice, which survived throughout the study period (60 days) with no tumor relapse (Figure 6C). Together, these findings clearly suggested that magneto-immunotherapy can elicit a strong abscopal effect to suppress the growth of distant tumors. Thus, the method developed in this study has the potential to treat metastatic cancers.

We further investigated the mechanisms underlying the abscopal effect observed. We first analyzed the tumor-infiltrating lymphocyte profiles in the untreated tumors. Mice with bilateral MC-38 tumors were treated as described in Figure 6A. On Day 17 (i.e., 10 days after treating the primary tumor), the secondary tumors without any treatment were harvested for flow cytometry analysis. The gating strategies are presented in Supplementary Figure S12. Figure 6D,E show that the percentage of $CD3^+CD8^+$ T cells in the secondary tumors dramatically increased in the mice receiving magnetotherapy (IONC−AAPH with AMF) or magneto-immunotherapy (IONC−AAPH with AMF plus ICB). There was no significant difference between these two groups (Figure 6D,E). These results suggest that treating the primary tumor with magneto-therapy can increase the number of $CD3^+CD8^+$ T cells in the untreated secondary tumor. We further evaluated the tumor-specific immune response post magneto-immunotherapy by enzyme-linked immunospot (ELISpot) assay. The splenocytes were harvested on Day 17 and stimulated for 24 h with KSPWFTTL, a tumor-associated antigen (TAA) peptide. Splenocytes incubated with ovalbumin (OVA) peptide SINFEKL or without peptide were included as control groups. As shown in Figure 6F,G, the number of antigen-specific IFN-γ producing T cells was significantly higher in the mice treated with magneto-immunotherapy (668 ± 93 per 10^6 cells), which was 4.5- and 2.8-fold higher than that of the saline control (148 ± 44 per 10^6 cells) and magnetotherapy (235 ± 126 per 10^6 cells) groups, respectively. Our results indicate that magneto-immunotherapy of primary tumor can efficiently activate systemic tumor-specific T-cell response. Thus, the strong abscopal effect of magneto-immunotherapy may result from the combination of increased tumor infiltrating $CD8^+$ T cells and enhanced tumor-specific T-cell response.

Magneto-Immunotherapy Induced Long-Term Immune Memory. Immune memory is the hallmark of the adaptive immune response essential for long-term protection against pathogens including tumor cells. Upon a second encounter with the same tumor cells, memory T cells can rapidly respond and mount a much stronger and more effective immune response than the first immune response. We therefore investigated if IONC−AAPH under AMF could induce immune memory against tumor rechallenge. The first tumor was inoculated by subcutaneous injection of MC-38 cells into the right flank of the C57BL/6N mouse (Supplementary Figure 13A). When the tumor volume reached 50−100 mm^3, the tumors were removed by 1−2 rounds of treatment. The mice treated with magneto-immunotherapy (IONC−AAPH with AMF and ICB) were intraperitoneally injected with anti-PD-1 antibody (10 mg/kg of body weight) 1, 4, and 7 days after the first round of magnetotherapy. After the first tumors were completely eradicated, the mice were housed for additional 40 days to allow the possible establishment of immune memory. They were then rechallenged with MC-38 cells on the contralateral side (Supplementary Figure 13A). Three naïve mice (without previous tumor implant) were inoculated with MC-38 cells and used as a control. As shown in Supplementary Figure 13B, the tumors in the naïve mice grew rapidly and reached the end point within 24 days, while the growth of the second tumors in the mice treated with IONC−AAPH under AMF were completely inhibited or significantly delayed. Two out of three mice rejected the tumor rechallenge. Excitingly, all the three mice cured by magneto-immunotherapy (IONC−AAPH + AMF + anti-PD-1) completely rejected the tumor rechallenge and survived throughout the study period (Supplementary Figure 13B). No tumor relapse occurred over a year post the magneto-immunotherapy. These findings clearly demonstrated that IONC−AAPH under AMF induced long-term protective immune memory against the tumors.

Evaluation of Toxicity of IONC−AAPH. To evaluate the potential toxicity of IONC−AAPH, we first examined the *in vivo* biodistribution of IONC−AAPH by Prussian blue iron staining. The IONC−AAPH was directly injected into the tumor, and the tumor was completely eradicated by IONC−AAPH under AMF. As shown in Supplementary Figure S14, the iron staining was only found in the tumor-draining lymph node (TDLN) and the spleen, which might be due to transportation within the lymphatic system. No IONC was found in the contralateral inguinal lymph node and other vital organs (Supplementary Figure S14). We also monitored the mouse body weight, examined the morphology of vital organs, and evaluated the indices of liver and kidney functions. We found that there were no large fluctuations of body weight in IONC−AAPH-treated mice (Supplementary Figure S15). The mice behaved normally after the treatment. The results of histological examination showed that there was no morphological change or apparent injury in the vital organs (Supplementary Figure S16). Compared with the control mice, there was no significant difference in the blood levels of alanine transaminase (ALT), aspartate aminotransferase (AST), alkaline phosphatase (ALP), blood urea nitrogen (BUN), and creatinine in IONC−AAPH treated mice (Supplementary Figure S17), suggesting that there was no adverse effect on the liver and kidney functions. Together, these findings indicate that IONC−AAPH is biocompatible and the magneto-immunotherapy using IONC−AAPH is safe.

CONCLUSIONS

In summary, we developed a magneto-immunotherapy for solid tumors by combining magnetic iron oxide nanocluster (IONC) based heat and free radical generation with immune checkpoint blockade therapy. Upon applying an alternating magnetic field, the IONCs produce a high level of local heat, decomposing the attached AAPH molecules, resulting in carbon-centered free radicals. We showed that the simultaneous generation of heat and free radicals from IONC−AAPH effectively killed tumor cells by causing intracellular GSH depletion and damaging multiple cellular components including DNA, actin cytoskeleton, mitochondria, and lipid membranes. The tumor cell death caused by combined magnetic heating and free radicals is highly immunogenic, as demonstrated by cell surface translocation of CRT and Hsp70, and release of ATP, which promoted dendritic cell maturation. Treating the primary tumors with IONC−AAPH under AMF led to the eradication of the tumors. Further, the combination

https://doi.org/10.1021/acsnano.2c06776
ACS Nano 2022, 16, 18538−18554

of IONC−AAPH under AMF with anti-PD-1 ICB dramatically inhibited the growth of untreated distant tumors by inducing tumor-specific T cell response and increasing tumor-infiltrating $CD8^+$ T cells. In addition, this magneto-immunotherapy also induced a strong long-term immune memory effect against tumor rechallenge. Hence, the IONC−AAPH-based magneto-immunotherapy has the potential to effectively control cancer recurrence and combat cancer metastasis, thus significantly improving the current cancer therapies.

METHODS

Materials. Ethylene glycol (anhydrous, 99.8%), iron(III) chloride hexahydrate ($FeCl_3·6H_2O$, ACS reagent, 97%), urea (ACS reagent, 99.0%), azobis(isobutyronitrile) (AIBN, 98%), acrylic acid (anhydrous, contains 200 ppm MEHQ as inhibitor, 99%), 2-acrylamido-2-methylpropanesulfonic acid (AMPS, 99%), dimethylformamide (DMF, anhydrous, 99.8%), 3,4-dihydroxyphenethylamine hydrochloride (dopamine), poly(ethylene glycol) methyl ether methacrylate (M_w 500), poly(acrylic acid) (PAA, M_w ∼ 1,800), sodium nitrite (ACS reagent, ≥97.0%), 2,2′-azobis(2-methylpropionamidine) dihydrochloride (AAPH) and lipid peroxidation detection kit were purchased from Sigma-Aldrich. 1-Ethyl-3-(3-(dimethylamino)-propyl)carbodiimide hydrochloride (EDC), sulfuric acid (ACS grade, 98%), hydrochloric acid (ACS grade, 37%), 2,2′-azino-bis(3-ethylbenzothiazoline-6-sulfonic acid (ABTS) solution, 2′,7′-dichlorodihydrofluorescein diacetate (H_2DCFDA), calcein acetoxymethyl ester (Calcein AM), bicinchoninic acid (BCA) protein assay kit, Alexa Fluor 568 Phalloidin, Hoechst 33342, JC-1 Dye, and Alexa Fluor 594 TUNEL assay kit were purchased from Thermo Fisher Scientific. Polyacrylic acid sodium salt (PAA, M_w ∼ 6,000) was purchased from Polyscience Inc. Alexa Fluor 488 conjugated calreticulin antibody, Alexa Fluor 488 conjugated Ki-67 antibody, FITC conjugated CD3 antibody, and γ-H2AX antibody were obtained from Cell Signaling Technology. APC-conjugated CD4 antibody, PE-conjugated CD8α antibody, PE-conjugated CD11c antibody, FITC-conjugated CD80 antibody, APC-conjugated CD86 antibody, CD16/CD32 antibody, and fixable viability stain 450 were purchased from BD Biosciences. Iron staining kit, creatinine quantification kit, mouse aspartate aminotransferase (AST) ELISA kit, recombinant mouse granulocyte-macrophage colony-stimulating factor (GM-CSF), HIF-1α antibody, GAPDH antibody, FITC conjugated Hsp70 antibody, horseradish peroxidase (HRP)-conjugated goat antirabbit secondary antibody, Alexa Fluor 488 conjugated goat antirabbit antibody, and DAPI-containing mounting medium were purchased from Abcam. ATP and GSH quantification kits were obtained from Promega. The ELISA kits for quantification of mouse alanine transaminase (ALT), alkaline phosphatase (ALP), and blood urea nitrogen (BUN) were obtained from MyBioSource. $OVA_{257–264}$ peptide (SINFEKL) and MC-38 tumor-associated antigen peptide MuLV p15E (KSPWFTTL) were purchased from MBL. Mouse Hsp70 ELISA and mouse IFN-γ ELISpot kits were purchased from R&D Systems. Propidium iodide (Anaspec), annexin V apoptosis kit (SouthernBiotech), mycoplasma detection kit (Lonza), anti-PD-1 antibody (InvivoGen), and 4-compartment cell culture dishes (Greiner bio-one) were purchased from the indicated sources, respectively.

Synthesis of Iron Oxide Nanocrystal Clusters. Iron oxide nanocrystal clusters (IONCs) were synthesized using a solvothermal method described in the literature.[43] Briefly, $FeCl_3·6H_2O$ (540 mg), PAA (250 mg), urea (1200 mg), and deionized water (Milli-Q, >18 mΩ, 1.5 mL) were dissolved in ethylene glycol (20 mL) using a magnetic stirrer. This reaction mixture was vigorously stirred for 60 min, leading to a transparent yellow solution. The solution was then transferred to the Teflon-lined stainless steel autoclave reactor. The reactor was heated at 200 °C for 6 h in an oven. A black solution was obtained after cooling down the reaction solution, indicating the formation of iron oxide nanocrystal clusters. The clusters were collected using a rare earth magnet. The product was washed by a mixture of acetone and water six times to remove the byproducts and unreacted reactants. The purified clusters were redispersed in water for further use.

Replacement of PAA on IONC Surface by Dopamine. Five milliliters of dopamine aqueous solution (1 mg/mL) was added to 5 mL of IONC solution (1 mg Fe/mL) in a 20 mL glass vial. The mixture was stirred for 2 h. The mixture became turbid gradually during stirring, indicating the replacement of the polyacrylate by dopamine. The aggregated clusters were collected magnetically using a rare earth magnet. The sample was washed 6 times with water to remove free dopamine.

Synthesis of Poly(AA-*co*-AMPS-*co*-PEG). The copolymer was synthesized using the free radical polymerization method. Briefly, PEG-acrylate (1.0 g), AMPS (0.75 g), acrylic acid (0.25 g), and AIBN (300 mg) were dissolved in 10 mL of DMF in a 20 mL glass vial. The vial was then transferred to an oven equipped with an ultraviolet illumination lamp (LZC-4Xb photoreactor, UVA 350 nm). The mixture was magnetically stirred for 4 h under ultraviolet radiation to form polymers. The obtained polymer was purified using a dialysis bag (Cellulose Membrane, MWCO 3 kDa) to remove impurities. Then the purified copolymer was dried for 2 days using a freeze-dryer.

Grafting Poly(AA-*co*-AMPS-*co*-PEG) onto Clusters. Poly(AA-*co*-AMPS-*co*-PEG) was grafted to IONC surface through EDC conjugation under sonication. Typically, 2 mL of the copolymer solution (40 mg/mL), 1 mL of MES buffer solution (0.5 mol/L), and 1 mL of EDC solution (20 mg/mL) were added to the aggregated clusters (5 mL, 1 mg Fe/mL). The mixture of the copolymer and the clusters was then sonicated for 30 min using a probe sonicator. The poly(AA-*co*-AMPS-*co*-PEG) functionalized clusters were washed magnetically 5 times using water to remove impurities.

Synthesis of Nitrodopamine. Nitrodopamine was synthesized following a method reported in the literature.[43] Briefly, 5 g of dopamine hydrochloride was dissolved in 150 mL of deionized water under vigorous magnetic stirring. Then 6.5 g of sodium nitrate was added to the solution, and then the mixture was cooled to 0 °C using an ice bath. Fifty milliliters of 20% sulfuric acid was added to the mixture very slowly. The ice bath was removed after the addition of sulfuric acid. The reaction mixture was stirred at room temperature overnight. Nitrodopamine hydrogensulfate was collected by filtering the reaction dispersion. The product was washed with cold water six times to remove the byproducts and impurities. The purified product was freeze-dried and stored at 4 °C for further use.

Synthesis of Polymer Nitrodopamine-PAA-AAPH. The polymer of nitro-dopamine-PAA-AAPH was synthesized through EDC conjugation. Aqueous solution of PAA (0.36 mL, 50 mg/mL), MES (0.5 mL, 1 M), EDC (3.2 mL, 10 mg/mL) and 5.48 mL of deionized water were mixed under vigorous stirring. Aqueous solution of EDC (3.2 mL, 10 mg/mL) was added to the solution and the mixture was stirred vigorously at room temperature for 5 min. Aqueous solution of nitro-dopamine (2.96 mL, 2 mg/mL) was added to the solution, and the mixture was stirred for another 15 min. Then AAPH in 50 mM MES solution (10 mL, 100 mg/mL) was added to the reaction mixture. The reaction mixture was stirred for 3 more hours to attach AAPH molecules to the chain of PAA. The polymer was purified using a stirred cell (MWCO 3 kDa) to remove unreacted reactants and byproducts.

Attachment of Nitrodopamine-PAA-AAPH to IONC Surface. Nitrodopamine-PAA-AAPH was attached to the cluster surface through the coordination between the functional group of catechol on nitrodopamine and iron atoms on the surface of clusters. Freshly purified nitro-dopamine-PAA-AAPH solution (10 mL, 1 mM) and IONC (10 mL, 1 mg Fe/mL) were mixed at 4 °C. The mixture was mechanically shaken at 4 °C for 3 h. Then the clusters were purified using stirred cell (MWCO 500 kDa) to remove the free polymers.

Material Characterizations. Transmission electron microscopy (TEM) image and high-resolution TEM (HRTEM) image of the clusters were acquired using a JEOL 2100 Field Emission Gun Transmission Electron Microscope at an acceleration voltage of 200 kV. A drop of the cluster solution was evaporated on a carbon-coated copper grid to prepare the TEM sample. The average diameter of the clusters was calculated from measurement of at least five hundred

https://doi.org/10.1021/acsnano.2c06776
ACS Nano 2022, 16, 18538−18554

clusters. The Fourier-transform infrared (FTIR) spectra of the clusters were obtained on an IR Affinity-1S FTIR spectrometer (Shimadzu). The samples were washed eight times to remove free AAPH prior to FTIR measurement. One milliliter of a cluster solution with a concentration of 500 mg Fe/L was dropped onto the center of a glass slide. The slide was dried at 60 °C to form a thin layer of residue. The spectra were collected from 4000 to 400 cm^{-1} at room temperature. The hydrodynamic diameter of the clusters was measured using a Wyatt Technology's Mobius dynamic light scattering instrument. The average size was obtained over three measurements for each sample. The surface area of the cluster was measured using a Quantachrome Autosorb-iQ3-MP/Kr BET Surface analyzer. Prior to the measurement, the samples were outgassed overnight under vacuum at 200 °C.

Magnetic Measurements. The magnetic properties of the clusters were measured using a superconducting quantum interference device (Quantum Design MPMS). The nanocrystals were dispersed in calcium sulfate at a weight ratio of approximately 1% to prevent sample movement and to reduce magnetic coupling among the nanocrystals. To calculate the mass magnetization accurately, the iron content of the samples was directly measured from the pellets after the measurements. The pellets were digested with 5 mL of 12 M hydrochloric acid, and the iron concentration of the solutions was measured by a ferrozine assay.

Cell Culture. MC-38 cells were purchased from Kerafast. The cells were maintained in Dulbecco's Modified Eagle Medium (DMEM) supplemented with 10% fetal bovine serum (FBS) at 37 °C in a humidified atmosphere with 5% CO_2. The cells were routinely tested using mycoplasma detection kit.

Detection of $ABTS^{+\bullet}$ Free Radicals. The generation of $ABTS^{+\bullet}$ free radicals was achieved via the reaction between ABTS solution and IONC−AAPH or IONC in PBS. 250 μL of ABTS solution was mixed with 250 μL of PBS containing IONC or IONC−AAPH of 300 μg Fe/mL concentration. The mixture was shielded from light and incubated at 37 °C or under an AMF (H = 9.35 kA/m and f = 320 kHz) for 1 h. After incubation, the nanoclusters in the mixture were removed using Vivaspin centrifugal filters (MWCO 100 kDa). The absorbance of the samples containing $ABTS^{+\bullet}$ free radicals was measured from 400 to 950 nm with a microplate reader (Tecan Spark Multimode Microplate Reader).

Detection of Intracellular Free Radicals. The intracellular generation of free radicals was determined using H_2DCFDA probe. Briefly, MC-38 cells were seeded in 4-compartment CELLview cell culture dishes (1×10^5 cells per compartment). Twenty-four hours later, the cells were incubated with IONC−AAPH or IONC at 300 μg Fe/mL for 1 h at 37 °C. After incubation, the cells were exposed to AMF for 1 h. Then the cells were washed twice with PBS and stained with 2 μM of H_2DCFDA at 37 °C for 30 min. The generation of free radicals was observed using a fluorescence microscope (ZOE Fluorescent Cell Imager, Bio-Rad) or quantified via flow cytometry (BD Accuri C6 Plus).

Quantification of Intracellular Iron Oxide Nanocrystals. The intracellular iron oxide nanocrystals were quantified using a ferrozine-based colorimetric assay. MC-38 cells were incubated with IONC or IONC−AAPH at 300 μg Fe/mL for 1 h at 37 °C. After incubation, the extracellular nanocrystals were removed. The cells were washed with PBS, detached with trypsin, and pelleted by centrifugation. The cell pellets were dried under vacuum and treated with 50 μL of HCl (12 M) to release intracellular iron. Then, 70 μL of NaOH (8 M), 100 μL of ammonium acetate (4 M), 100 μL of hydroxylamine HCl (5% w/w), 680 μL of water, and 1 mL of ferrozine (0.1% w/w) were added sequentially. The iron content was determined by light absorbance at 562 nm.

Examination of Cell Viability. Cell viability was evaluated via fluorescence imaging or flow cytometry. MC-38 cells were seeded in 4-compartment cell culture dishes and incubated overnight. To mimic hypoxic conditions, the cells were pretreated with 100 μM $CoCl_2$ for 24 h. Then 300 μg Fe/mL of IONC−AAPH or IONC was added to the cell culture medium. The cells were then exposed to AMF for 2 h followed by live/dead staining. The temperature of the cell culture medium was measured in real time with a fiber-optic temperature probe (Photon Control). For fluorescence imaging, the cells were costained with calcein AM (3 μM) and propidium iodide (5 μM) at 37 °C for 30 min. The images were taken using ZOE Fluorescent Cell Imager. For flow cytometry analysis, the cells were detached and stained with Annexin V Apoptosis Kit following the manufacturer's instructions. Data were collected on BD Accuri C6 Plus flow cytometer and analyzed using FlowJo software (Tree Star).

Western Blot Analysis. $CoCl_2$-induced hypoxia in MC-38 cells was confirmed by Western blot analysis of HIF-1α. MC-38 cells were treated with 100 μM $CoCl_2$ for 24 h at 37 °C. The cells were lysed with RIPA buffer containing protease inhibitors (Thermo Fisher Scientific). The protein concentration of the cell lysate was quantified using BCA assay. The proteins were resolved by SDS-PAGE and transferred to a polyvinylidene fluoride (PVDF) membrane (Bio-Rad). The membrane was blocked with 5% nonfat milk and probed with HIF-1α and GAPDH antibodies followed by HRP-conjugated secondary antibodies. The target proteins were visualized using enhanced chemiluminescent HRP substrate (Thermo Fisher Scientific). The protein levels were quantified using ImageJ software.

Detection of DNA Damage. The DNA damage induced by IONC−AAPH treatment was detected by γ-H2AX staining. MC-38 cells were seeded in 4-compartment cell culture dishes and cultured overnight. Then the cells were treated with 300 μg Fe/mL of IONC−AAPH or IONC at 37 °C or under AMF for 90 min. Four hours after the treatment, the cells were fixed with 4% paraformaldehyde for 20 min, permeabilized with 0.2% Triton X-100 for 20 min and blocked with 3% bovine serum albumin (BSA) for 30 min at room temperature. Then the cells were stained with an antibody against γ-H2AX at 4 °C overnight followed by staining with an Alexa Fluor 488-labeled secondary antibody for 2 h at room temperature. The nuclei were stained with Hoechst 33342 for 10 min at room temperature. The cells were imaged with a Nikon A1-Rsi confocal microscope and the fluorescence intensity of γ-H2AX was analyzed with ImageJ software.

Evaluation of F-Actin Morphology. The F-actin morphology of MC-38 cells was evaluated by phalloidin staining. MC-38 cells were seeded in 4-compartment cell culture dishes and cultured overnight. The cells were then treated with 300 μg Fe/mL of IONC−AAPH or IONC at 37 °C or under AMF for 90 min. Four hours after the treatment, the cells were fixed, permeabilized, and blocked as described above in the Detection of DNA Damage section. Then the cells were incubated with Alexa Fluor 568-labeled phalloidin for 30 min at room temperature, followed by staining with Hoechst 33342 for 10 min at room temperature. Images were collected using a Nikon A1-Rsi confocal microscope.

Determination of Mitochondrial Health. The mitochondrial membrane potential of MC-38 cells was determined with JC-1 staining assay. MC-38 cells cultured in 4-compartment cell culture dishes were treated with 300 μg Fe/mL of IONC−AAPH or IONC at 37 °C or under AMF for 90 min. Four hours post the treatment, the cells were stained with JC-1 dye at 10 μg/mL at 37 °C for 20 min. After staining, the cells were imaged with a confocal microscope (Nikon A1-Rsi confocal) or analyzed on a flow cytometer (BD Accuri C6 Plus). The ratio of J-aggregates to J-monomers was calculated using the red and green fluorescence intensity measured by flow cytometry.

Quantification of Intracellular GSH. MC-38 cells were seeded in 4-compartment cell culture dishes at a density of 1×10^5 cells per compartment and cultured overnight. Then the cells were treated with 300 μg Fe/mL of IONC−AAPH or IONC at 37 °C or under AMF for 2 h. Two hours after the treatment, the culture medium was removed and the intracellular GSH was quantified using a luminescence-based GSH-Glo Glutathione Assay according to the manufacturer's instructions.

Determination of Lipid Peroxidation. The lipid peroxidation of MC-38 cells was determined by measuring the production of malondialdehyde (MDA). MC-38 cells cultured in 4-compartment cell culture dishes were treated with 300 μg Fe/mL of IONC−AAPH or IONC at 37 °C or under AMF for 2 h. Two hours post the treatment, the cells were lysed, and the MDA levels were quantified

https://doi.org/10.1021/acsnano.2c06776
ACS Nano 2022, 16, 18538−18554

using a fluorescence-based MDA Assay Kit following the manufacturer's instructions.

Detection of Damage-Associated Molecular Patterns. Damage-associated molecular patterns (DAMPs), including calreticulin (CRT), heat shock protein 70 (Hsp70), and adenosine triphosphate (ATP), were analyzed at different time points after the treatment. Briefly, MC-38 cells were seeded in 4-compartment cell culture dishes at a density of 1×10^5 cells per compartment and cultured overnight. Then the cells were treated with 300 μg Fe/mL of IONC−AAPH or IONC at 37 °C or under AMF for 2 h. To detect CRT and Hsp70 exposure on cell surface, the cells were detached 2 and 6 h after the treatment and stained with fluorophore-conjugated anti-CRT or anti-Hsp70 antibody on ice for 30 min. Then the cells were analyzed by flow cytometry. To determine ATP release induced by the treatment, the cell culture medium was collected 2 and 6 h post the treatment. The extracellular ATP was quantified using an ATP bioluminescence detection kit following the manufacturer's instructions. To determine the change in Hsp70 expression, the cells were lysed 24 h post the treatment. The expression of Hsp70 was quantified by ELISA and normalized to total protein.

Determination of Dendritic Cell Maturation. The bone marrow-derived dendritic cells (BMDCs) were prepared from the bone marrow of 8-week old C57BL/6N mice according to an established protocol.[67] To determine the stimulatory effect on BMDCs, IONC−AAPH-treated MC-38 cells (together with the medium containing DAMPs) were cocultured with BMDCs for 24 h in a transwell system (pore size = 3 μm). BMDCs only (without coculture) were included as the blank groups. The BMDCs were collected, blocked with CD16/CD32 antibody, and stained with PE-CD11c, FITC-CD80, and APC-CD86. The data were acquired on MA900 Multi-Application Cell Sorter (Sony) and analyzed using FlowJo software (Tree Star).

Tumor Killing Effect of IONC−AAPH *In Vivo*. All animal work was approved by the Institutional Animal Care and Use Committee (IACUC) of Rice University. C57BL/6N mice (4−6 weeks, female) were purchased from Charles River Laboratories. The direct tumor killing effect of IONC−AAPH treatment was evaluated with subcutaneous tumor-bearing mice. Briefly, 5×10^5 MC-38 cells were subcutaneously injected into the right flank of the mice. The mice were randomly divided into 6 groups (n = 3): saline, AAPH, IONC, IONC−AAPH, IONC + AMF, and IONC−AAPH + AMF. When the tumor volume reached 150−200 mm^3, the mice were administrated with saline, AAPH (2 mM), IONC (5 mg Fe/mL), or IONC−AAPH (5 mg Fe/mL) through intratumoral injection at a speed of 3 μL/min using a syringe pump (World Precision Instruments). The injection volume was 0.3 μL per mm^3 tumor tissue. The mice in IONC + AMF and IONC−AAPH + AMF groups were treated with AMF (H = 9.35 kA/m and f = 320 kHz) for 1 h. A customized polycarbonate cradle with a heating pad was placed underneath the mice to maintain the body temperature during anesthesia. The temperature in the tumor was measured using a high-resolution infrared (IR) camera (E95, Teledyne FLIR). The tumor size was measured daily with a digital caliper, and the tumor volume was calculated as follow: volume = length × width^2/2.

Twenty-four hours after the treatment, the tumor tissues were collected for H&E, Ki-67, and TUNEL staining. At the end of the study, blood samples were collected for quantification of ALT, AST, ALP, BUN, and creatinine. The tumors were excised, weighed, and photographed. The major organs, including heart, lung, liver, spleen, and kidney, were harvested and examined by H&E staining. These organs together with the tumor-draining and the contralateral nondraining inguinal lymph nodes were examined for iron distribution by Prussian blue iron staining.

Abscopal Effect. The abscopal effect was determined with mice bearing bilateral subcutaneous tumors. 5×10^5 and 1×10^5 MC-38 cells were injected into the right and left flanks of the mice. The tumor on the right side was designated as the primary tumor for IONC−AAPH treatment, and the tumor on the left side was designated as the secondary (distant) tumor without IONC−AAPH treatment. The mice were randomly divided into 6 groups (n = 8): saline, anti-PD-1, IONC−AAPH, IONC−AAPH + anti-PD-1, IONC−AAPH + AMF, and IONC−AAPH + AMF + anti-PD-1. When the volume of the primary tumor reached 50−100 mm^3, saline or IONC−AAPH (7.5 mg Fe/mL) was injected directly into the primary tumor using the syringe pump. The injection volume was 0.3 μL per mm^3 tumor tissue. The mice in IONC−AAPH + AMF and IONC−AAPH + AMF + anti-PD-1 groups were treated with AMF for 1 h. 1, 4, and 7 days after the treatment, the mice in IONC−AAPH + AMF + anti-PD-1 group were administrated with anti-PD-1 antibody (10 mg/kg) through intraperitoneal (IP) injection. The anti-PD-1 antibody was also administrated to the mice in anti-PD-1 and IONC−AAPH + anti-PD-1 groups following the same schedule. The tumor sizes were measured daily with a digital caliper, and the tumor volume was calculated as follows: volume = length × width^2/2. For survival analysis, the mice were euthanized when the tumors reached the maximum permitted size (15 mm in any dimension) and counted as dead.

Flow Cytometry Analysis of Immune Cells in Untreated Distant Tumors. The tumor implantation and treatments were performed as described above in the Abscopal Effect section. On Day 17 (10 days after the first treatment), the distant tumors were collected for flow cytometry analysis of tumor infiltrating lymphocytes. Briefly, the tumor tissue was minced into small pieces and digested with 300 U/mL collagenase, 100 U/mL hyaluronidase, and 0.15 mg/mL DNase I (Stem Cell Technology) at 37 °C for 30 min under gentle shaking. The tumor tissue was then transferred to a 70 μm nylon mesh strainer to remove large pieces of undigested tissue. The cells filtered through the strainer were treated with ammonium chloride solution to remove red blood cells. Then the single-cell suspensions were incubated with anti-CD16/CD32 to block nonspecific binding to Fc receptors. The cells were further stained with the viability dye and fluorophore-conjugated antibodies against CD3 (FITC), CD4 (APC), and CD8 (PE). The data were acquired on MA900 Multi-Application Cell Sorter (Sony) and analyzed using FlowJo software (Tree Star).

IFN-γ ELISpot Assay. The tumor implantation and treatments were performed as described above in the Abscopal Effect section. On Day 17 (10 days after the first treatment), the mouse spleens were harvested from different treatment groups for the preparation of single-cell suspensions. The splenocytes (2×10^5 cells per well) were seeded into a 96-well plate precoated with anti-IFN-γ antibody. The cells were incubated with or without SINFEKL (OVA peptide) or KSPWFTTL (tumor-associated antigen peptide) at 10 μg/mL for 24 h at 37 °C. The ELISpot assay was performed using the Mouse IFN-γ ELISpot Kit (R&D Systems) according to the manufacturer's instructions. The IFN-γ spots were counted manually under a stereomicroscope.

Immune Memory Effect. The immune memory effect was investigated by rechallenging the surviving mice with MC-38 cells. Briefly, 5×10^5 MC-38 cells were first transplanted into the right flank of the mice. The mice were randomly divided into 2 groups: IONC−AAPH + AMF and IONC−AAPH + AMF + anti-PD-1. When the tumor volume reached 50−100 mm^3, the tumors were injected with IONC−AAPH (7.5 mg/mL) and treated with AMF for 1 h. The treatment was repeated once if the tumor was not completely removed by the first round of IONC−AAPH treatment. The mice in the IONC−AAPH + AMF + anti-PD-1 group were administrated with anti-PD-1 antibody (10 mg/kg of body weight) 1, 4, and 7 days after the first round of IONC−AAPH treatment. 40 days after the first tumor was removed, the mice were rechallenged by transplanting 5×10^5 MC-38 cells into the left flank. The tumor growth was monitored daily. A group of naïve mice (without previous tumor implant) were transplanted with 5×10^5 MC-38 cells in the left flank for comparison of tumor growth rate.

Statistical Analysis. All data are presented as mean ± s.d. or mean ± s.e.m. Statistical analysis was performed using GraphPad Prism (v8.0). Statistical tests are indicated in the figure legends. P values are indicated by asterisks in the figures as $^*P < 0.05$, $^{**}P < 0.01$, $^{***}P < 0.001$, and $^{****}P < 0.0001$. $P < 0.05$ was considered statistically significant.

https://doi.org/10.1021/acsnano.2c06776
ACS Nano 2022, 16, 18538−18554

ASSOCIATED CONTENT

Supporting Information

The Supporting Information is available free of charge at https://pubs.acs.org/doi/10.1021/acsnano.2c06776.

Quantification of $ABTS^{+\bullet}$; quantification of intracellular free radicals; HIF-1α expression in cells under hypoxia; confocal images of mitochondrial depolarization; translocation of calreticulin and Hsp70 onto cell surface; quantification of Hsp70 expression; gating strategies for analyzing DC maturation and TILs; *in vivo* temperature measurement; individual tumor growth curve; immune memory effect; biodistribution of IONCA-AAPH; body weight; H&E staining of major organs; evaluation of liver and kidney functions (PDF)

AUTHOR INFORMATION

Corresponding Author

Gang Bao − *Department of Bioengineering, Rice University, Houston, Texas 77030, United States;* orcid.org/0000-0001-5501-554X; Email: gang.bao@rice.edu

Authors

Linlin Zhang − *Department of Bioengineering, Rice University, Houston, Texas 77030, United States;* orcid.org/0000-0003-3240-1215

Qingbo Zhang − *Department of Bioengineering, Rice University, Houston, Texas 77030, United States;* orcid.org/0000-0001-8289-0227

Daniel T. Hinojosa − *Department of Bioengineering, Rice University, Houston, Texas 77030, United States*

Kaiyi Jiang − *Department of Bioengineering, Rice University, Houston, Texas 77030, United States;* orcid.org/0000-0002-9569-5225

Quoc-Khanh Pham − *Department of Bioengineering, Rice University, Houston, Texas 77030, United States*

Zhen Xiao − *Department of Chemistry, Brown University, Providence, Rhode Island 02912, United States;* orcid.org/0000-0002-3740-3546

Vicki L. Colvin − *Department of Chemistry, Brown University, Providence, Rhode Island 02912, United States;* orcid.org/0000-0002-8526-515X

Complete contact information is available at: https://pubs.acs.org/10.1021/acsnano.2c06776

Author Contributions

#L.Z. and Q.Z. contributed equally to this work. L.Z., Q.Z., and G.B. conceived the idea, designed the study, and wrote the manuscript, with comments from all coauthors. L.Z., Q.Z., D.H., K.J., and Q.P. performed experiments and data analysis. Z.X. and V.C. provided materials.

Notes

The authors declare no competing financial interest.

ACKNOWLEDGMENTS

This work was supported by the Cancer Prevention and Research Institute of Texas (RP220518 to G.B.).

REFERENCES

(1) Sung, H.; Ferlay, J.; Siegel, R. L.; Laversanne, M.; Soerjomataram, I.; Jemal, A.; Bray, F. Global Cancer Statistics 2020: GLOBOCAN Estimates of Incidence and Mortality Worldwide for 36 Cancers in 185 Countries. *CA Cancer J. Clin* **2021**, *71*, 209−249.

(2) Sauer, S.; Reed, D. R.; Ihnat, M.; Hurst, R. E.; Warshawsky, D.; Barkan, D. Innovative Approaches in the Battle Against Cancer Recurrence: Novel Strategies to Combat Dormant Disseminated Tumor Cells. *Front Oncol* **2021**, *11*, 659963.

(3) Steeg, P. S. Targeting metastasis. *Nat. Rev. Cancer* **2016**, *16*, 201−18.

(4) Shekhar, M. P. Drug resistance: challenges to effective therapy. *Curr. Cancer Drug Targets* **2011**, *11*, 613−23.

(5) Tannock, I. F. Conventional cancer therapy: promise broken or promise delayed? *Lancet* **1998**, *351* (Suppl 2), SII9−16.

(6) Waldman, A. D.; Fritz, J. M.; Lenardo, M. J. A guide to cancer immunotherapy: from T cell basic science to clinical practice. *Nat. Rev. Immunol* **2020**, *20*, 651−668.

(7) Hargadon, K. M.; Johnson, C. E.; Williams, C. J. Immune checkpoint blockade therapy for cancer: An overview of FDA-approved immune checkpoint inhibitors. *Int. Immunopharmacol* **2018**, *62*, 29−39.

(8) Pitt, J. M.; Vetizou, M.; Daillere, R.; Roberti, M. P.; Yamazaki, T.; Routy, B.; Lepage, P.; Boneca, I. G.; Chamaillard, M.; Kroemer, G.; Zitvogel, L. Resistance Mechanisms to Immune-Checkpoint Blockade in Cancer: Tumor-Intrinsic and -Extrinsic Factors. *Immunity* **2016**, *44*, 1255−69.

(9) Rosenberg, S. A.; Restifo, N. P. Adoptive cell transfer as personalized immunotherapy for human cancer. *Science* **2015**, *348*, 62−8.

(10) Sebestyen, Z.; Prinz, I.; Déchanet-Merville, J.; Silva-Santos, B.; Kuball, J. Translating gammadelta ($\gamma\delta$) T cells and their receptors into cancer cell therapies. *Nat. Rev. Drug Discov* **2020**, *19*, 169−184.

(11) Edwards, S. C.; Hoevenaar, W. H. M.; Coffelt, S. B. Emerging immunotherapies for metastasis. *Br. J. Cancer* **2021**, *124*, 37−48.

(12) Zappasodi, R.; Merghoub, T.; Wolchok, J. D. Emerging Concepts for Immune Checkpoint Blockade-Based Combination Therapies. *Cancer Cell* **2018**, *33*, 581−598.

(13) Heinhuis, K. M.; Ros, W.; Kok, M.; Steeghs, N.; Beijnen, J. H.; Schellens, J. H. M. Enhancing antitumor response by combining immune checkpoint inhibitors with chemotherapy in solid tumors. *Ann. Oncol* **2019**, *30*, 219−235.

(14) Procureur, A.; Simonaggio, A.; Bibault, J. E.; Oudard, S.; Vano, Y. A. Enhance the Immune Checkpoint Inhibitors Efficacy with Radiotherapy Induced Immunogenic Cell Death: A Comprehensive Review and Latest Developments. *Cancers (Basel)* **2021**, *13*, 678.

(15) Li, Z.; Deng, J.; Sun, J.; Ma, Y. Hyperthermia Targeting the Tumor Microenvironment Facilitates Immune Checkpoint Inhibitors. *Front Immunol* **2020**, *11*, 595207.

(16) Ng, C. W.; Li, J. C.; Pu, K. Y. Recent Progresses in Phototherapy-Synergized Cancer Immunotherapy. *Adv. Funct Mater.* **2018**, *28*, 1804688.

(17) Yagawa, Y.; Tanigawa, K.; Kobayashi, Y.; Yamamoto, M. Cancer immunity and therapy using hyperthermia with immunotherapy, radiotherapy, chemotherapy, and surgery. *J. cancer metastatis treat* **2017**, *3*, 218−230.

(18) Chen, Q.; Xu, L.; Liang, C.; Wang, C.; Peng, R.; Liu, Z. Photothermal therapy with immune-adjuvant nanoparticles together with checkpoint blockade for effective cancer immunotherapy. *Nat. Commun.* **2016**, *7*, 13193.

(19) Nam, J.; Son, S.; Ochyl, L. J.; Kuai, R.; Schwendeman, A.; Moon, J. J. Chemo-photothermal therapy combination elicits anti-tumor immunity against advanced metastatic cancer. *Nat. Commun.* **2018**, *9*, 1074.

(20) Peng, J.; Xiao, Y.; Li, W.; Yang, Q.; Tan, L.; Jia, Y.; Qu, Y.; Qian, Z. Photosensitizer Micelles Together with IDO Inhibitor Enhance Cancer Photothermal Therapy and Immunotherapy. *Adv. Sci. (Weinh)* **2018**, *5*, 1700891.

(21) Wang, C.; Xu, L.; Liang, C.; Xiang, J.; Peng, R.; Liu, Z. Immunological responses triggered by photothermal therapy with carbon nanotubes in combination with anti-CTLA-4 therapy to inhibit cancer metastasis. *Adv. Mater.* **2014**, *26*, 8154−62.

(22) Deng, X.; Shao, Z.; Zhao, Y. Solutions to the Drawbacks of Photothermal and Photodynamic Cancer Therapy. *Adv. Sci. (Weinh)* **2021**, *8*, 2002504.
(23) Cazares-Cortes, E.; Cabana, S.; Boitard, C.; Nehlig, E.; Griffete, N.; Fresnais, J.; Wilhelm, C.; Abou-Hassan, A.; Menager, C. Recent insights in magnetic hyperthermia: From the "hot-spot" effect for local delivery to combined magneto-photo-thermia using magneto-plasmonic hybrids. *Adv. Drug Deliv Rev.* **2019**, *138*, 233−246.
(24) Chao, Y.; Chen, G.; Liang, C.; Xu, J.; Dong, Z.; Han, X.; Wang, C.; Liu, Z. Iron Nanoparticles for Low-Power Local Magnetic Hyperthermia in Combination with Immune Checkpoint Blockade for Systemic Antitumor Therapy. *Nano Lett.* **2019**, *19*, 4287−4296.
(25) Liu, X.; Zheng, J.; Sun, W.; Zhao, X.; Li, Y.; Gong, N.; Wang, Y.; Ma, X.; Zhang, T.; Zhao, L. Y.; Hou, Y.; Wu, Z.; Du, Y.; Fan, H.; Tian, J.; Liang, X. J. Ferrimagnetic Vortex Nanoring-Mediated Mild Magnetic Hyperthermia Imparts Potent Immunological Effect for Treating Cancer Metastasis. *ACS Nano* **2019**, *13*, 8811−8825.
(26) Pan, J.; Xu, Y.; Wu, Q.; Hu, P.; Shi, J. Mild Magnetic Hyperthermia-Activated Innate Immunity for Liver Cancer Therapy. *J. Am. Chem. Soc.* **2021**, *143*, 8116−8128.
(27) Noh, S. H.; Moon, S. H.; Shin, T. H.; Lim, Y.; Cheon, J. Recent advances of magneto-thermal capabilities of nanoparticles: From design principles to biomedical applications. *Nano Today* **2017**, *13*, 61−76.
(28) Maluta, S.; Romano, M.; Dall'oglio, S.; Genna, M.; Oliani, C.; Pioli, F.; Gabbani, M.; Marciai, N.; Palazzi, M. Regional hyperthermia added to intensified preoperative chemo-radiation in locally advanced adenocarcinoma of middle and lower rectum. *Int. J. Hyperthermia* **2010**, *26*, 108−17.
(29) Van Loenhout, J.; Peeters, M.; Bogaerts, A.; Smits, E.; Deben, C. Oxidative Stress-Inducing Anticancer Therapies: Taking a Closer Look at Their Immunomodulating Effects. *Antioxidants (Basel)* **2020**, *9*, 1188.
(30) Song, W.; Kuang, J.; Li, C. X.; Zhang, M. K.; Zheng, D. W.; Zeng, X.; Liu, C. J.; Zhang, X. Z. Enhanced Immunotherapy Based on Photodynamic Therapy for Both Primary and Lung Metastasis Tumor Eradication. *ACS Nano* **2018**, *12*, 1978−1989.
(31) Xie, J.; Gong, L.; Zhu, S.; Yong, Y.; Gu, Z.; Zhao, Y. Emerging Strategies of Nanomaterial-Mediated Tumor Radiosensitization. *Adv. Mater.* **2019**, *31*, e1802244.
(32) Xu, J.; Xu, L.; Wang, C.; Yang, R.; Zhuang, Q.; Han, X.; Dong, Z.; Zhu, W.; Peng, R.; Liu, Z. Near-Infrared-Triggered Photodynamic Therapy with Multitasking Upconversion Nanoparticles in Combination with Checkpoint Blockade for Immunotherapy of Colorectal Cancer. *ACS Nano* **2017**, *11*, 4463−4474.
(33) Yin, Y. F.; Jiang, X. W.; Sun, L. P.; Li, H. Y.; Su, C. X.; Zhang, Y.; Xu, G.; Li, X. L.; Zhao, C. K.; Chen, Y.; Xu, H. X.; Zhang, K. Continuous inertial cavitation evokes massive ROS for reinforcing sonodynamic therapy and immunogenic cell death against breast carcinoma. *Nano Today* **2021**, *36*, 1804688.
(34) Rakotomalala, A.; Escande, A.; Furlan, A.; Meignan, S.; Lartigau, E. Hypoxia in Solid Tumors: How Low Oxygenation Impacts the "Six Rs" of Radiotherapy. *Front Endocrinol* **2021**, *12*, 17.
(35) Ming, L.; Cheng, K.; Chen, Y.; Yang, R.; Chen, D. Enhancement of tumor lethality of ROS in photodynamic therapy. *Cancer Med.* **2021**, *10*, 257−268.
(36) Shen, Y.; Dong, C.; Xiang, H.; Li, C.; Zhuang, F.; Chen, Y.; Lu, Q.; Chen, Y.; Huang, B. Engineering Oxygen-Irrelevant Radical Nanogenerator for Hypoxia-Independent Magnetothermodynamic Tumor Nanotherapy. *Small Methods* **2021**, *5*, e2001087.
(37) Huang, G.; Qiu, Y.; Yang, F.; Xie, J.; Chen, X.; Wang, L.; Yang, H. Magnetothermally Triggered Free-Radical Generation for Deep-Seated Tumor Treatment. *Nano Lett.* **2021**, *21*, 2926−2931.
(38) Shen, S.; Zhu, C.; Huo, D.; Yang, M.; Xue, J.; Xia, Y. A Hybrid Nanomaterial for the Controlled Generation of Free Radicals and Oxidative Destruction of Hypoxic Cancer Cells. *Angew. Chem., Int. Ed. Engl.* **2017**, *56*, 8801−8804.
(39) Wang, X. Q.; Gao, F.; Zhang, X. Z. Initiator-Loaded Gold Nanocages as a Light-Induced Free-Radical Generator for Cancer Therapy. *Angew. Chem., Int. Ed. Engl.* **2017**, *56*, 9029−9033.
(40) Li, F. J.; Kondo, T.; Zhao, Q. L.; Hayashi, Y.; Ogawa, R.; Cui, Z. G.; Feril, L. B. A lipophilic free radical initiator, 2,2′-azobis (2,4-dimethylvaleronitrile) (AMVN) enhances caspase-dependent apoptosis induced by hyperthermia. *Int. J. Hyperther* **2003**, *19*, 165−177.
(41) Yuki, H.; Kondo, T.; Zhao, Q. L.; Fujiwara, Y.; Tanabe, K.; Ogawa, R.; Nakashima, A.; Fushiki, H.; Fujimura, M.; Saito, S. A free radical initiator, 2,2′-azobis (2-aminopropane) dihydrochloride enhances hyperthermia-induced apoptosis in human uterine cervical cancer cell lines. *Free Radic. Res.* **2003**, *37*, 631−643.
(42) Wang, C. C.; Chen, F.; Kim, E.; Harrison, L. E. Thermal sensitization through ROS modulation: A strategy to improve the efficacy of hyperthermic intraperitoneal chemotherapy. *Surgery* **2007**, *142*, 384−392.
(43) Xiao, Z.; Zhang, Q.; Guo, X.; Villanova, J.; Hu, Y.; Külaots, I.; Garcia-Rojas, D.; Guo, W.; Colvin, V. L. Libraries of Uniform Magnetic Multicore Nanoparticles with Tunable Dimensions for Biomedical and Photonic Applications. *ACS Appl. Mater. Interfaces* **2020**, *12*, 41932−41941.
(44) Werber, J.; Wang, Y. J.; Milligan, M.; Li, X. H.; Ji, J. A. Analysis of 2,2′-Azobis (2-Amidinopropane) Dihydrochloride Degradation and Hydrolysis in Aqueous Solutions. *J. Pharm. Sci.* **2011**, *100*, 3307−3315.
(45) Munoz-Sanchez, J.; Chanez-Cardenas, M. E. The use of cobalt chloride as a chemical hypoxia model. *J. Appl. Toxicol* **2019**, *39*, 556−570.
(46) Oei, A. L.; Vriend, L. E. M.; Crezee, J.; Franken, N. A. P.; Krawczyk, P. M. Effects of hyperthermia on DNA repair pathways: one treatment to inhibit them all. *Radiat Oncol* **2015**, *10*, 13.
(47) White, M. G.; Luca, L. E.; Nonner, D.; Saleh, O.; Hu, B.; Barrett, E. F.; Barrett, J. N., Cellular mechanisms of neuronal damage from hyperthermia. In *Neurobiology of Hyperthermia*; Sharma, H. S., Ed.; Elsevier Science Bv: Amsterdam, 2007; Vol. *162*, pp 347−371.
(48) Liu, J. Y.; Kang, L.; Ratnayake, I.; Ahrenkiel, P.; Smith, S.; Wang, C. Z. Targeting cancer cell adhesion molecule, CD146, with low-dose gold nanorods and mild hyperthermia disrupts actin cytoskeleton and cancer cell migration. *J. Colloid Interface Sci.* **2021**, *601*, 556−569.
(49) Yuki, H.; Kondo, T.; Zhao, Q. L.; Fujiwara, Y.; Tanabe, K.; Ogawa, R.; Nakashima, A.; Fushiki, H.; Fujimura, M.; Saito, S. A free radical initiator, 2,2′-azobis (2-aminopropane) dihydrochloride enhances hyperthermia-induced apoptosis in human uterine cervical cancer cell lines. *Free Radic Res.* **2003**, *37*, 631−643.
(50) Ivashkevich, A.; Redon, C. E.; Nakamura, A. J.; Martin, R. F.; Martin, O. A. Use of the gamma-H2AX assay to monitor DNA damage and repair in translational cancer research. *Cancer Lett.* **2012**, *327*, 123−33.
(51) Nagelkerke, A.; Span, P. N., Staining Against Phospho-H2AX (gamma-H2AX) as a Marker for DNA Damage and Genomic Instability in Cancer Tissues and Cells. In *Tumor Microenvironment: Study Protocols*, Koumenis, C., Coussens, L. M., Giaccia, A., Hammond, E., Eds.; Springer International Publishing Ag: Cham, 2016; Vol. *899*, pp 1−10.
(52) Nagelkerke, A.; van Kuijk, S. J. A.; Martens, J. W.; Sweep, F.; Hoogerbrugge, N.; Bussink, J.; Span, P. N. Poor prognosis of constitutive gamma-H2AX expressing triple-negative breast cancers is associated with telomere length. *Biomark Med.* **2015**, *9*, 383−390.
(53) Sivandzade, F.; Bhalerao, A.; Cucullo, L. Analysis of the Mitochondrial Membrane Potential Using the Cationic JC-1 Dye as a Sensitive Fluorescent Probe. *Bio Protoc* **2019**, *9*, e3128.
(54) Forman, H. J.; Zhang, H. Q.; Rinna, A. Glutathione: Overview of its protective roles, measurement, and biosynthesis. *Mol. Aspects Med.* **2009**, *30*, 1−12.
(55) Kawamura, T.; Kondoh, Y.; Muroi, M.; Kawatani, M.; Osada, H. A small molecule that induces reactive oxygen species via cellular glutathione depletion. *Biochem. J.* **2014**, *463*, 53−63.

https://doi.org/10.1021/acsnano.2c06776
ACS Nano 2022, 16, 18538−18554

(56) Del Rio, D.; Stewart, A. J.; Pellegrini, N. A review of recent studies on malondialdehyde as toxic molecule and biological marker of oxidative stress. *Nutr Metab Cardiovasc Dis* **2005**, *15*, 316−328.
(57) Zhou, J.; Wang, G.; Chen, Y.; Wang, H.; Hua, Y.; Cai, Z. Immunogenic cell death in cancer therapy: Present and emerging inducers. *J. Cell Mol. Med.* **2019**, *23*, 4854−4865.
(58) Pallardy, M. J.; Turbica, I.; Biola-Vidamment, A. Why the Immune System Should Be Concerned by Nanomaterials? *Front Immunol* **2017**, *8*, 544.
(59) Yang, J. X.; Hou, M. F.; Sun, W. S.; Wu, Q. H.; Xu, J.; Xiong, L. Q.; Chai, Y. M.; Liu, Y. X.; Yu, M. H.; Wang, H. L.; Xu, Z. P.; Liang, X. W.; Zhang, C. F. Sequential PDT and PTT Using Dual-Modal Single-Walled Carbon Nanohorns Synergistically Promote Systemic Immune Responses against Tumor Metastasis and Relapse. *Adv. Sci.* **2020**, *7*, 2001088.
(60) Yang, J.; Xie, R.; Feng, L.; Liu, B.; Lv, R.; Li, C.; Gai, S.; He, F.; Yang, P.; Lin, J. Hyperthermia and Controllable Free Radical Coenhanced Synergistic Therapy in Hypoxia Enabled by Near-Infrared-II Light Irradiation. *ACS Nano* **2019**, *13*, 13144−13160.
(61) Kalluru, P.; Vankayala, R.; Chiang, C. S.; Hwang, K. C. Nano-graphene oxide-mediated In vivo fluorescence imaging and bimodal photodynamic and photothermal destruction of tumors. *Biomaterials* **2016**, *95*, 1−10.
(62) Dias, L. D.; Buzzá, H. H.; Stringasci, M. D.; Bagnato, V. S. Recent Advances in Combined Photothermal and Photodynamic Therapies against Cancer Using Carbon Nanomaterial Platforms for In Vivo Studies. *Photochem* **2021**, *1*, 434−447.
(63) Reynders, K.; Illidge, T.; Siva, S.; Chang, J. Y.; De Ruysscher, D. The abscopal effect of local radiotherapy: using immunotherapy to make a rare event clinically relevant. *Cancer Treat Rev.* **2015**, *41*, 503−10.
(64) Wang, M.; Song, J.; Zhou, F.; Hoover, A. R.; Murray, C.; Zhou, B.; Wang, L.; Qu, J.; Chen, W. R. NIR-Triggered Phototherapy and Immunotherapy via an Antigen-Capturing Nanoplatform for Metastatic Cancer Treatment. *Adv. Sci. (Weinh)* **2019**, *6*, 1802157.
(65) Liu, Y.; Dong, Y.; Kong, L.; Shi, F.; Zhu, H.; Yu, J. Abscopal effect of radiotherapy combined with immune checkpoint inhibitors. *J. Hematol Oncol* **2018**, *11*, 104.
(66) Ngwa, W.; Irabor, O. C.; Schoenfeld, J. D.; Hesser, J.; Demaria, S.; Formenti, S. C. Using immunotherapy to boost the abscopal effect. *Nat. Rev. Cancer* **2018**, *18*, 313−322.
(67) Dewitte, H.; Verbeke, R.; Breckpot, K.; Vandenbroucke, R. E.; Libert, C.; De Smedt, S. C.; Lentacker, I. Choose your models wisely: How different murine bone marrow-derived dendritic cell protocols influence the success of nanoparticulate vaccines in vitro. *J. Controlled Release* **2014**, *195*, 138−146.

https://doi.org/10.1021/acsnano.2c06776
ACS Nano 2022, 16, 18538−18554